Monthly Notices
of the
ROYAL ASTRONOMICAL SOCIETY

MNRAS **479,** 570–587 (2018)
Advance Access publication 2018 June 5

doi:10.1093/mnras/sty1455

SMHASH: anatomy of the Orphan Stream using RR Lyrae stars

David Hendel,[1★] Victoria Scowcroft,[2,3] Kathryn V. Johnston,[1] Mark A. Fardal,[4] Roeland P. van der Marel,[4,5] Sangmo T. Sohn,[4] Adrian M. Price-Whelan,[6] Rachael L. Beaton,[6†] Gurtina Besla,[7] Giuseppe Bono,[8,9] Maria-Rosa L. Cioni,[10] Giselle Clementini,[11] Judith G. Cohen,[12] Michele Fabrizio,[9,13] Wendy L. Freedman,[14] Alessia Garofalo,[11,15] Carl J. Grillmair,[16] Nitya Kallivayalil,[17] Juna A. Kollmeier,[3] David R. Law,[4] Barry F. Madore,[3] Steven R. Majewski,[17] Massimo Marengo,[18] Andrew J. Monson,[3] Jillian R. Neeley,[18] David L. Nidever,[19] Grzegorz Pietrzyński,[20] Mark Seibert,[3] Branimir Sesar,[21] Horace A. Smith,[22] Igor Soszyński[23] and Andrzej Udalski[23]

Affiliations are listed at the end of the paper

Accepted 2018 May 25. Received 2018 May 23; in original form 2017 November 10

ABSTRACT

Stellar tidal streams provide an opportunity to study the motion and structure of the disrupting galaxy as well as the gravitational potential of its host. Streams around the Milky Way are especially promising as phase space positions of individual stars will be measured by ongoing or upcoming surveys. Nevertheless, it remains a challenge to accurately assess distances to stars farther than 10 kpc from the Sun, where we have the poorest knowledge of the Galaxy's mass distribution. To address this, we present observations of 32 candidate RR Lyrae stars in the Orphan tidal stream taken as part of the *Spitzer* Merger History and Shape of the Galactic Halo (SMHASH) program. The extremely tight correlation between the periods, luminosities, and metallicities of RR Lyrae variable stars in the *Spitzer* IRAC 3.6 μm band allows the determination of precise distances to individual stars; the median statistical relative distance uncertainty to each RR Lyrae star is 2.5 per cent. By fitting orbits in an example potential, we obtain an upper limit on the mass of the Milky Way interior to 60 kpc of $5.6^{+1.2}_{-1.1} \times 10^{11}$ $M_{\odot}$, bringing estimates based on the Orphan Stream in line with those using other tracers. The SMHASH data also resolve the stream in line-of-sight depth, allowing a new perspective on the internal structure of the disrupted dwarf galaxy. Comparing with *N*–body models, we find that the progenitor had an initial dark halo mass of approximately 3.2×10^9 $M_{\odot}$, placing the Orphan Stream's progenitor amongst the classical dwarf spheroidals.

Key words: stars: variables: RR Lyrae – Galaxy: halo – Galaxy: kinematics and dynamics – Galaxy: structure.

1 INTRODUCTION

Tidal debris structures are striking evidence of hierarchical assembly – the premise that the Milky Way and systems like it have been built over cosmic time through the coalescence of many smaller objects (White & Rees 1978; Johnston, Hernquist & Bolte 1996; Bullock, Kravtsov & Weinberg 2001; Freeman & Bland-Hawthorn 2002). Some of this construction is in the form of major mergers, where two near-equal mass galaxies collide and their stars are redistributed wholesale as the new galaxy violently relaxes. However, in the prevailing Λ-cold dark matter (ΛCDM) model, the vast majority of mergers (by number) are minor (Fakhouri, Ma & Boylan-Kolchin 2010), where one halo, the host, dominates the interaction and a smaller object, the satellite, is dragged inward by dynamical friction and eventually stripped of mass by tidal forces. When the luminous component is disrupted the stars may form a stellar tidal stream or shell, depending on the parameters of the interaction (e.g.

★ E-mail: hendel@astro.columbia.edu
† Hubble Fellow.

Johnston et al. 2008; Amorisco 2015; Hendel & Johnston 2015). The study of tidal features therefore probes the accretion histories of galaxies.

Stellar tidal streams are also key tools for our current understanding of the Milky Way's gravitational potential. The techniques applied to measure the potential are wide-ranging but commonly a few-parameter potential model is varied in an attempt to match simulations to the available data. Historically, the streams used most often for this purpose are the Sagittarius dwarf galaxy's stream (Majewski et al. 2003; Law & Majewski 2010; Gibbons, Belokurov & Evans 2014) and various globular cluster streams such as Palomar 5 and GD-1 (Koposov, Rix & Hogg 2010;Fritz & Kallivayalil 2015; Küpper et al. 2015; Pearson et al. 2015; Bovy et al. 2016).

The Orphan tidal stream (Belokurov et al. 2006; Grillmair 2006) has several advantages over the other streams mentioned above. It forms a smooth arc that is significantly longer (detected length of $\approx$108°; Grillmair et al. 2015), wider ($\sim$2°; Belokurov et al. 2006), and farther from the Galactic centre (>50 kpc; Newberg et al. 2010; Sesar et al. 2013) than any of the commonly studied globular cluster streams. Along with its total luminosity ($M_r < -7.5$, Belokurov et al. 2007) and metallicity spread of 0.56 dex (Casey et al. 2013), these characteristics suggest a dwarf spheroidal galaxy as the likely origin, but the progenitor is elusive and possibly nearly completely disrupted by the Galaxy's tidal field (Grillmair et al. 2015). In contrast to the Sagittarius stream, the Orphan Stream has a uniform appearance and cold velocity structure; the Sagittarius stream is notoriously complex, featuring multiple wraps, bifurcated tails, and several stellar populations with different kinematics (Belokurov et al. 2006; Koposov et al. 2012; Gibbons, Belokurov & Evans 2017). The orbital planes of the Orphan and Sagittarius streams are misaligned by $\sim$67° (Pawlowski, Pflamm-Altenburg & Kroupa 2012), making the combination of the two an attractive target for multistream potential measuring methods (Sanderson, Helmi & Hogg 2015; Bovy et al. 2016).

The Orphan Stream also has the advantage of a well-filled horizontal branch resulting in numerous classes of stars that may be used as standard candles for distance estimation, for example the Blue Horizontal Branch (BHB) stars studied by Newberg et al. (2010). Of particular relevance to this work, the Orphan Stream contains a significant population of RR Lyrae stars (RRL), which have been the focus of several recent efforts to improve distance measurement into the Galactic halo (e.g. Hernitschek et al. 2017; Sesar et al. 2017). These stars make excellent standard candles using period–luminosity (PL) relations with their near- or mid-infrared magnitudes (Longmore, Fernley & Jameson 1986; Bono et al. 2001, 2003; Catelan, Pritzl & Smith 2004; Braga et al. 2015). In addition to the advantage of decreased extinction at these longer wavelengths compared to the V band ($A_V/A_{[3.6\,\mu m]} \sim 15$, Cardelli, Clayton & Mathis 1989; Indebetouw et al. 2005), the PL relation has also been shown to have a small intrinsic scatter in the infrared (Madore et al. 2013; Neeley et al. 2015; Muraveva et al. 2018). Recently these relations have been extended to include a metallicity component (Neeley et al. 2017) with the effect of further decreasing the uncertainty on individual stars' absolute magnitudes and thus removing scatter in measured distances for systems with a large range in metallicity, such as the Orphan Stream.

The *Spitzer* Merger History And Shape of the Galactic Halo (SMHASH) program builds upon the previous Carnegie RR Lyrae Program (CRRP; Freedman et al. 2012) to leverage these excellent distance indicators and explore a variety of Local Group substructures including five dwarf galaxies [Sagittarius, Sculptor (Garofalo et al. 2018), Ursa Minor, Carina, and Boötes] along with the Sagittarius and Orphan tidal streams. As we will show, the precision is such that we are able to resolve the three-dimensional structure of the stream, granting special access to a system that is in many ways the archetypal minor merger event.

In this work, we present *Spitzer Space Telescope* (Werner et al. 2004) Infrared Array Camera (IRAC; Fazio et al. 2004) 3.6 μm magnitudes and inferred distances to 32 candidate Orphan Stream RR Lyrae stars with the principal goal of informing future studies of the Galactic potential and Orphan Stream progenitor. In Section 2, we describe our *Spitzer* photometry and the calculation of apparent magnitudes. Section 3 describes how we derive distances to individual Orphan Stream stars. In Section 4, we define a procedure to fit orbits to the RRL and measure bulk properties of the stream; in Section 5, we investigate the extent to which the orbit fits place constraints on the mass of the Milky Way. Section 6 studies the Orphan progenitor and Section 7 concludes.

2 OBSERVATIONS AND DATA REDUCTION

2.1 Data selection

The RR Lyrae stars selected for observation in the SMHASH Orphan program are the 31 'high probability' candidate stream members of Sesar et al. (2013); these stars are all fundamental-mode pulsators (RRab). Also included is one 'medium probability' candidate, RR5, because it was measured at a large distance despite having a line-of-sight velocity somewhat discrepant with expectations for the Orphan Stream given its position. The stars were identified from a compilation of three synoptic sky surveys: the Catalina Real-Time Sky Survey (CRTS; Drake et al. 2009), the Lincoln Near Earth Asteroid Research (LINEAR; Stokes et al. 2000) survey, and the Palomar Transient Factory (PTF; Law et al. 2009; Rau et al. 2009). Sesar et al. (2013) obtained low-resolution follow-up spectroscopic observations in order to implement a Galactic standard of rest velocity cut as part of their stream membership criteria. All of our targets therefore have uniformly determined metallicity (on the Layden 1994 system, which is calibrated to the globular cluster metallicity scale of Zinn & West 1984) and line-of-sight velocity measurements with uncertainties of 0.15 dex and $\sim$15 km s^{-1}, respectively. Their catalogue number in Table 1 is in order of decreasing declination, which approximately corresponds to a sequence of increasing apparent magnitude and decreasing Heliocentric distance (see fig. 2 in Sesar et al. 2013).

2.2 *Spitzer* observations

The mid-infrared observations presented here were collected using the Infrared Array Camera (IRAC) on the *Spitzer* Space Telescope as part of the Warm *Spitzer* Cycle 10 between 2014 June 19 and 2015 August 31 (Johnston et al. 2013). Each star was observed in 12 epochs at 3.6 μm only.

The targets selected in the Orphan Stream span a wide range in distance and therefore cover a significant range in apparent infrared magnitude. In order to achieve a sufficient signal-to-noise ratio on the individual epochs for both the nearest and most distant targets, the stars were divided into two groups based on their distances from Sesar et al. (2013) and their anticipated apparent magnitude from the K-band PL relation. The closer, brighter targets (with estimated distances less than $\sim$40 kpc) were observed at each epoch with five dithered 100 s exposures, with all 12 epochs approximately

Table 1. Distances and light curve parameters of SMHASH Orphan RR Lyrae stars.

ID	R.A. (J2000)	Decl. (J2000)	Period (d)	HJD_0 [a] (d)	[3.6] mag [b] (mag)	[3.6] amp. (mag)	$A_{[3.6]}$ [c] (mag)	[Fe/H]	Helio. distance (kpc)
RR4	142.596 437	49.440 867	0.677 648	54265.667221	17.39 ± 0.01	0.16	0.003	−2.32	44.04 ± 1.06
RR5	139.486 634	49.043 981	0.595 984	54508.734151	17.79 ± 0.02	0.22	0.002	−2.05	48.88 ± 1.21
RR6	143.840 446	47.091 109	0.530 818	55887.972840	17.94 ± 0.03	0.34	0.002	−2.37	50.91 ± 1.36
RR7	141.771 831	46.359 489	0.639 017	55590.054047	17.67 ± 0.02	0.26	0.003	−1.94	47.27 ± 1.19
RR9	144.271 648	42.603 354	0.567 199	54913.653005	17.63 ± 0.02	0.22	0.002	−2.08	44.36 ± 1.10
RR10	142.541 300	42.570 500	0.649 151	54157.679811	17.70 ± 0.02	0.21	0.002	−2.53	50.62 ± 1.26
RR11	144.881 448	41.439 236	0.624 166	56271.888900	17.39 ± 0.02	0.20	0.002	−2.56	43.26 ± 1.07
RR12	146.057 798	40.220 714	0.711 552	56334.821312	17.21 ± 0.02	0.23	0.003	−2.35	41.61 ± 1.04
RR13	143.482 581	39.134 007	0.527 853	54415.904058	17.73 ± 0.02	0.19	0.002	−2.22	45.47 ± 1.11
RR14	143.913 227	38.853 250	0.504 139	53789.793479	18.00 ± 0.01	0.15	0.002	−2.36	51.21 ± 1.23
RR15	146.447 585	37.553 258	0.624 026	54913.654037	17.00 ± 0.02	0.18	0.002	−2.14	34.87 ± 0.85
RR16	148.586 324	37.191 956	0.573 213	54941.722401	17.52 ± 0.01	0.15	0.002	−2.18	42.81 ± 1.03
RR17	142.909 363	37.002 696	0.582 839	55598.766679	17.41 ± 0.02	0.18	0.002	−2.73	43.01 ± 1.05
RR18	146.008 547	36.265 846	0.594 436	53789.812373	17.30 ± 0.01	0.16	0.002	−2.27	39.53 ± 0.96
RR19[d]	146.390 649	35.795 310	0.755 026	52722.727848	16.85 ± 0.01	0.05	0.002	−1.96	34.92 ± 0.81
RR23	150.579 833	26.598 017	0.573 755	53078.770191	16.95 ± 0.03	0.31	0.004	−2.42	33.61 ± 0.89
RR24	150.243 511	25.826 153	0.708 142	54476.844880	16.63 ± 0.01	0.16	0.005	−2.14	31.17 ± 0.75
RR25	150.647 213	25.247 547	0.542 891	54539.656204	16.87 ± 0.02	0.20	0.005	−2.12	30.83 ± 0.76
RR26	151.892 507	24.831 492	0.620 861	53788.855568	16.83 ± 0.02	0.23	0.006	−2.09	32.09 ± 0.80
RR27	150.544 334	24.257 983	0.604 737	54595.657970	16.82 ± 0.02	0.27	0.005	−1.86	30.89 ± 0.79
RR29	153.996 368	19.222 735	0.645 174	53816.785913	16.50 ± 0.02	0.23	0.004	−2.00	27.84 ± 0.70
RR30	153.698 975	19.125 864	0.630 652	54149.788097	16.35 ± 0.02	0.18	0.005	−2.09	25.86 ± 0.63
RR31	154.238 008	18.790 623	0.508 603	52648.880186	16.33 ± 0.02	0.24	0.005	−1.97	23.06 ± 0.58
RR32	154.824 925	18.226 018	0.578 446	54084.925828	16.73 ± 0.02	0.22	0.005	−1.61	28.42 ± 0.70
RR33	154.469 145	17.427 796	0.575 995	54207.717695	16.84 ± 0.02	0.22	0.005	−1.75	30.16 ± 0.75
RR34	154.295 002	17.131 504	0.513 222	53706.970133	16.66 ± 0.02	0.25	0.005	−1.88	26.71 ± 0.67
RR35	156.791 313	15.992 450	0.592 709	54175.771290	16.45 ± 0.02	0.25	0.005	−2.32	26.84 ± 0.68
RR39	158.493 827	9.235 715	0.554 073	53851.699888	16.34 ± 0.02	0.22	0.004	−2.00	24.13 ± 0.60
RR43	160.996 538	3.565 153	0.618 892	53710.968168	16.64 ± 0.02	0.23	0.006	−2.31	29.87 ± 0.75
RR46	161.045 184	0.876 656	0.591 287	54535.792607	16.70 ± 0.03	0.30	0.007	−1.58	28.26 ± 0.73
RR47	161.622 376	0.491 299	0.463 190	54180.766355	16.34 ± 0.02	0.26	0.006	−1.50	21.31 ± 0.54
RR49	162.349 340	−2.609 458	0.523 622	53054.827672	16.30 ± 0.02	0.25	0.006	−2.02	23.05 ± 0.58

[a] Reduced Heliocentric Julian Date of maximum brightness (HJD – 2400000)
[b] Extinction-corrected, flux-averaged 3.6 μm apparent magnitude from GLOESS fit (Section 2.4)
[c] 3.6 μm extinction from the Schlafly & Finkbeiner (2011) dust map, calculated by http://irsa.ipac.caltech.edu/applications/DUST/
[d] RR19 is likely not an RR Lyrae star (or a member of the Orphan Stream) but we include it here for completeness.

uniformly spaced over a single pulsation cycle. The more distant, fainter targets used 25 dithered 100 s exposures to obtain the required S/N ratio. However, given the longer exposure times and the short pulsation cycle of the RRL, it was not possible to schedule all 12 observations within a single pulsation cycle. Instead these observations are spaced non-uniformly over several cycles, with typically 8–10 d between the first and last observation of a given target.

2.3 Photometry

Individual Basic Calibrated Data (BCDs) generated by IRAC pipeline version S19.2 were downloaded from the *Spitzer* Science Center (SSC). Mosaics were created with the SSC-provided software MOPEX (Makovoz & Khan 2005); both individual- and all-epoch ('master') mosaics for each field were produced with a 0.6 arcsec pixel scale. Point spread function (PSF) photometry was performed using the DAOPHOT/ALLSTAR/ALLFRAME program suite (Stetson 1987, 1994). Further details of the SMHASH photometric procedure will be provided in an upcoming work (Garofalo et al. 2018).

The Orphan Stream is highly diffuse so crowding from other stream members is not important, but we find PSF photometry useful regardless to eliminate any contribution from field stars aligned by chance with the RRL. PSF stars were required to appear in at least 75 per cent of dithers and were chosen from uncrowded stars as determined by visual examination. For each target, the PSF made from the epoch 1 mosaic is used on all epochs. Experiments with several stars showed no difference in measured magnitudes when using a PSF made from epoch 1, the master mosaic, or individual PSFs for each epoch.

The photometry was calibrated to the IRAC Vega magnitude system using the standard IRAC aperture correction procedure on the master mosaics, with inner and outer aperture radii of 6 and 14 pixels, respectively. Location corrections were applied to adjust for pixel-to-pixel sensitivity variations using the Warm Mission array location-correction images following the procedure outlined in the Warm *Spitzer* analysis documentation.[1]

[1] http://irsa.ipac.caltech.edu/data/SPITZER/docs/irac/

2.4 Light curves and average magnitudes

The phase-folded light curves for each of our observed stars, using the period and time of maximum brightness determined from the optical data (Table 1), are presented in Fig. A1; a subset is shown in Fig. 1. Each light curve is repeated for 3 phase cycles to highlight the variability. Stars where the telescope's scheduling resulted in multiple samples of the same point in phase (e.g. RR9, RR18) underscore *Spitzer's* precision photometric capabilities; the measured magnitudes of field stars have typical root-mean-squared variations of 0.03 mag between epochs, somewhat less than their mean single-epoch photometric uncertainty. The single-epoch magnitudes measured for each RRL are provided as an electronic supplement to this article. These have magnitude uncertainties of approximately 0.03 mag for the nearby subset and 0.02 mag for the farther subset which, while fainter, received an effective integration that was five times longer. Combined with the fact that (in each subset) the uncertainty decreases approximately with the square root of the flux, we conclude that photon count statistics are likely the dominant source of photometric uncertainty.

A smooth light curve is obtained from the observations using the Gaussian Local Estimation (GLOESS; Persson et al. 2004) algorithm. This technique evaluates the magnitude at a point in phase by fitting a second-order polynomial to the data, whose contributions to the fit are inversely weighted by the combination of both their statistical uncertainties and Gaussian distance from the point of interest. We use a Gaussian window of width 0.25 (in phase); the flux-averaged magnitude obtained from the fitted curve is not at all sensitive ($\Delta m = 1$–3×10^{-4} mag) to this smoothing length for any reasonable choice. The GLOESS light curve is used to determine the time-averaged, intensity-weighted mean magnitude. We compute the uncertainty on this quantity by adding in quadrature the per-star average photometric error and the uncertainty on the mean magnitude of the fitted light curve,

$$\sigma_{[3.6]} = \sqrt{\frac{\Sigma \sigma_i^2}{N^2} + \sigma_{\rm fit}^2}, \quad (1)$$

where N is the number of observations, σ_i is an individual epoch's photometric uncertainty, and $\sigma_{\rm fit}$ is the uncertainty on the average magnitude calculated from the GLOESS fit. The latter is dependent on the observing scheme; one can show that the uncertainty on mean magnitude decreases as $1/N$ if the light curve is sampled uniformly, in contrast to the slower $1/\sqrt{N}$ drop for data that has been randomly sampled (Freedman et al. 2012). Following the method of Scowcroft et al. (2011), we take advantage of this property where appropriate and compute $\sigma_{\rm fit} = A/(N\sqrt{12})$ for the brighter, uniformly sampled stars and $\sigma_{\rm fit} = A/(\sqrt{12N})$ for the fainter, non-uniformly observed subset, where A is the amplitude of the GLOESS light curve. Table 1 compiles the SMHASH mean magnitudes calculated in this way along with the archival data.

2.5 Membership and contamination

One of the principal difficulties in the study of halo substructure is separating tracers belonging to the object of interest from the background of halo objects of the same type. While the surveys contributing to the Orphan RRL catalogue are expected to be >95 per cent complete (Sesar et al. 2013), partitioning the objects into members and contaminants is key to drawing any conclusions from them. For this study of the Orphan Stream in particular, the issue is further complicated by one of Sagittarius' tails crossing the survey area around Galactic longitude $l \sim 200^\circ$; fortunately the Sagittarius debris is offset from the Orphan Stream in heliocentric radial velocity by $\sim$200 km s^{-1} in this part of the sky (e.g. Law, Johnston & Majewski 2005). This section discusses several heuristics that may be used to differentiate individual populations.

A typical way of separating stellar systems is identifying characteristic patterns in their chemical abundances left by their star formation histories. Unfortunately, the SMHASH Orphan Stream sample has a mean [Fe/H] of -2.1 dex and a dispersion of about 0.25 dex, which is not distinguishable from either the sample of stars in Sesar et al. (2013) whose kinematics are inconsistent with stream membership or RR Lyrae stars more generally in the smooth halo (mean [Fe/H] ~ -1.6, $\sigma \sim 0.3$, Drake et al. 2013). The mean metallicity can be used, however, to estimate how many Orphan Stream stars we should expect in the survey area. Using the universal dwarf galaxy luminosity–metallicity (LZ) relation obtained by Kirby et al. (2013) and the Orphan Stream K-giant metallicity of -1.63 ± 0.19 from Casey et al. (2013) (which should be more representative than the metal-poor RRL), we calculate that the progenitor should have had a luminosity $L_V \sim 1.6 \times 10^6\,L_\odot$. Sanderson (2016) found that the quantity $\log_{10} N_{\rm RRLy}/L_\odot$ is linear in metallicity with a scatter of 0.64 dex, which, when combined with the luminosity estimate, implies that the Orphan debris system has of order 100 RRL – with an uncertainty of $\sim$0.7 dex. Given that our precursor catalogues likely only cover one tail of the stream and that there are approximately 20 stars without spectra that Sesar et al. (2013) find are consistent with the stream's distance, we conclude that the observed RRL population is appropriate given the probable progenitor.

Next we consider the contribution of a principal contaminant population – the smooth stellar halo. For some time, it has been known that the number density of halo RR Lyrae stars sharply decreases at a Galactocentric distance of approximately 25 kpc (Saha 1985). More recent studies have shown that the power law index of this decline is $n = -4.5$ or greater (Keller et al. 2008; Watkins et al. 2009; Sesar et al. 2010; Cohen et al. 2017a). This is a significant advantage for studies of substructures beyond about 30 kpc as contaminants from the smooth component become almost negligible. For the case of the SMHASH Orphan footprint in particular, using the latest density normalization from Sesar et al. (2010), we expect only about 4 halo interlopers between 30 and 40 kpc and only 2 between 40 and 50 kpc. It is unlikely that a smooth halo star would also match the large radial velocity of the stream; a variety of halo tracers including RRL have measured velocity dispersions of $\sim$100 km s^{-1} (Wilhelm et al. 1999; Xue et al. 2008; Brown et al. 2010; Cohen et al. 2017b), comparable to the mean Galactic standard of rest velocities of our sample, which suppresses the expected number of contaminants by an additional factor of approximately four. The catalogue star RR5 was marked as a medium-probability member for precisely this reason – distant at 49 kpc but discrepant in radial velocity by 100 km s^{-1}.

There is also a subset of RRL that we do not expect to find as part of the Orphan Stream: high amplitude short period (HASP) RRab stars. These are fundamental mode pulsators that have large amplitudes, $A_V \geq 0.75$ mag, and periods less than approximately 0.48 d. RR Lyrae variables in dwarf spheroidal galaxies do not populate this part of the period–amplitude plane, possibly because their metallicity evolution is too slow to produce a component both old enough and metal rich enough to pulsate in this range (Bersier & Wood 2002; Fiorentino et al. 2015). The smooth halo does, however, contain stars in the HASP parameter space at the several percent level and therefore such stars are likely contaminants. Amongst the SMHASH Orphan sample only RR47 meets the HASP criteria; it

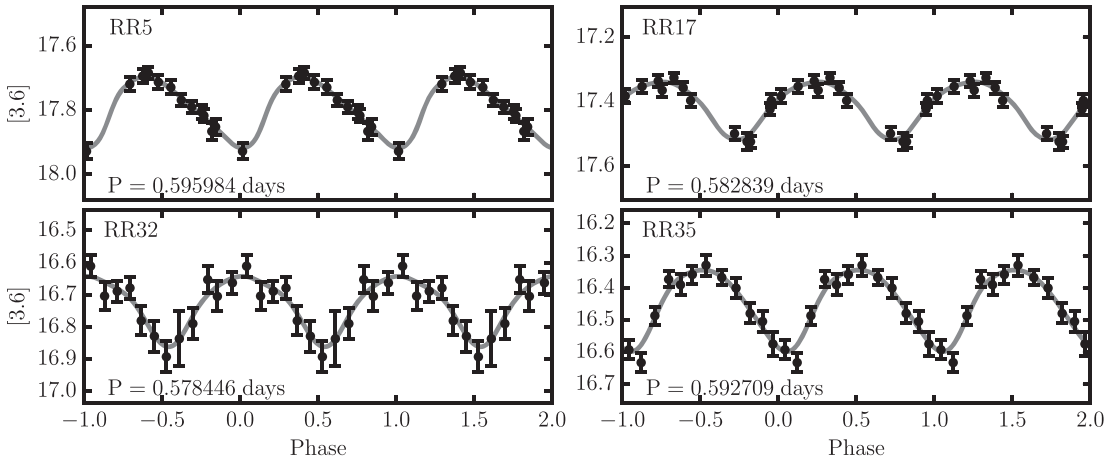

Figure 1. Four example 3.6 μm SMHASH RRL light curves. Each is repeated for three phase cycles to highlight their periodic behaviour. The remainder are displayed in Fig. A1. The infrared light curves display a more sinusoidal shape than the sharply peaked and skewed optical light curves, as expected. This subset demonstrates the difference in phase coverage between the near and far subsamples; the more distant stars (RR5, RR17) may have substantial gaps resulting from the telescope's scheduling but often also smaller uncertainties in individual measurements due to the larger number of BCDs per epoch.

is also at the smallest distance from the Galactic centre, where the smooth halo is more dominant as described above. Since it has not yet been proven that the Orphan Stream's progenitor was a dwarf spheroidal galaxy we do not exclude RR47 from the following dynamical analysis but note that the conclusions are not substantively changed if it is omitted.

We can, of course, use our 3.6 μm data to identify non-RRL contaminants. Examination of the light curve for RR19 leads us to believe that it is not, in fact, an RRL. This star was observed over a single presumed period (as determined from the optical data) but there is no evidence of coherent variability. The optical light curve from LINEAR, folded at the catalogue period, shows what might best be described as 'bursty' variability, which is also inconsistent with being an RRL. Investigating this further, we performed our own period search on the LINEAR data and found no significant periods consistent with being an RRab for this star. We posit that this may simply be a false positive in the database. RR19 is therefore excluded from the rest of our analysis, however we include it in Table 1 and Fig. A1 for completeness.

Finally, the recent *Gaia* Data Release 2 (Gaia Collaboration et al. 2016, 2018) source catalogue contains entries for each of the SMHASH Orphan Stream stars. As expected from pre-release estimates, the RRL considered here are too distant to have well-constrained parallaxes and too faint to have radial velocities measured in DR2. Most have measured proper motions that are broadly consistent with expectations for the Orphan Stream (see Section 4) with the clear exception of RR19; given the recorded $(\mu_\alpha, \mu_\delta) = (-3.5 \pm 0.3, -8.8 \pm 0.2)$ mas yr^{-1}, its transverse motion would be more than an order of magnitude larger than the others if it were at the same distance, validating its rejection as an interloper. The remaining RRL have typical relative proper motion uncertainties of 90 per cent (and even these may be systematically underestimated, c.f. Arenou et al. 2018; Lindegren et al. 2018). The most suspect of these are RR31, RR43, RR46, RR47, and RR49, which are also among the closest to the Galactic centre. However, to further clean the sample of contamination using the proper motions would require a highly model-dependent and iterative process. We defer this to future work to allow an equitable comparison with previous studies of the Orphan Stream and maintain focus on the precise distances provided by *Spitzer*.

3 DISTANCES TO THE ORPHAN RR LYRAE STARS

Distances to each of the Orphan RRL are determined using the (RRab-only) theoretical period–luminosity–metallicity (PLZ) relation of Neeley et al. (2017). They derived the PLZ using non-linear, time-dependent convective hydrodynamical models of RR Lyrae variables with a range of metal abundances. They found that fitting those models with a simple PL relation results in an 'intrinsic' scatter of ∼0.13 mag, whereas including a metallicity term reduces the scatter to ∼0.035 mag. The absolute magnitude in IRAC 3.6 μm is given by

$$M_{[3.6]} = -2.276(\pm0.021)\log(P) + 0.184(\pm0.004)[\mathrm{Fe/H}] - 0.786(\pm0.007). \quad (2)$$

We fully propagate all sources of uncertainty, including those from the photometry, the light curve fit, the constants in the PLZ relation including its intrinsic scatter, the measured metallicities, and the extinction in this band, $A_{[3.6]}$. The latter is calculated from the Schlafly & Finkbeiner (2011) dust map.[2] Because the extinction is very low, ∼0.005 mag, the entire value is adopted as the uncertainty on extinction. This conservative choice negligibly affects the resultant uncertainty on $M_{[3.6]}$.

The SMHASH Orphan Stream sample's relative distance uncertainty distribution is shown in Fig. 2. The median relative distance uncertainty is a mere 2.5 per cent. It is interesting to consider which, if any, of the observational uncertainties most strongly limit the precision of SMHASH distances. An elementary analysis of the error budget suggest that the metallicity uncertainty and Z-term slope contribute 0.5 per cent, the photometric and fit uncertainties contribute 0.9 per cent, and the intrinsic scatter, period slope and zero point are responsible for 1.1 per cent of the 2.5 per cent relative uncertainty. The heliocentric distances derived for each RRL using the Neeley et al. (2017) PLZ relation are given in Table 1.

Fig. 3 shows the RRLs' heliocentric distances as a function of Galactic longitude. We trace the stream to approximately 51 kpc. This figure makes it apparent that the Orphan Stream is not 'thin' at

[2]Evaluated using http://irsa.ipac.caltech.edu/applications/DUST/

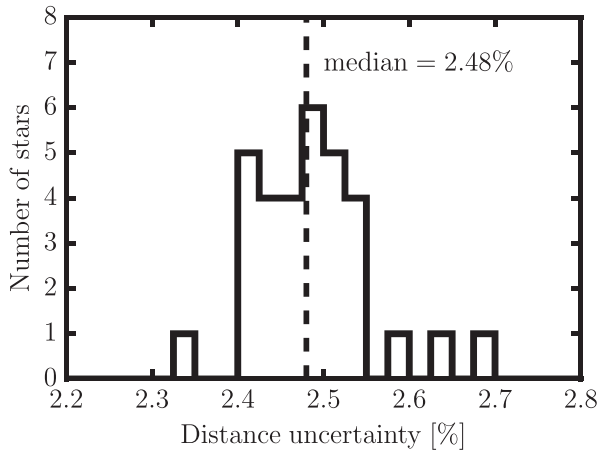

Figure 2. Relative heliocentric distance uncertainties σ_d/d for the SMHASH Orphan RRL. The median uncertainty is indicated by the vertical dashed line. The scatter in the PLZ relation and the uncertainty on apparent magnitudes each contribute ∼1 per cent, with the uncertainty in the star's individual metallicities providing the remainder.

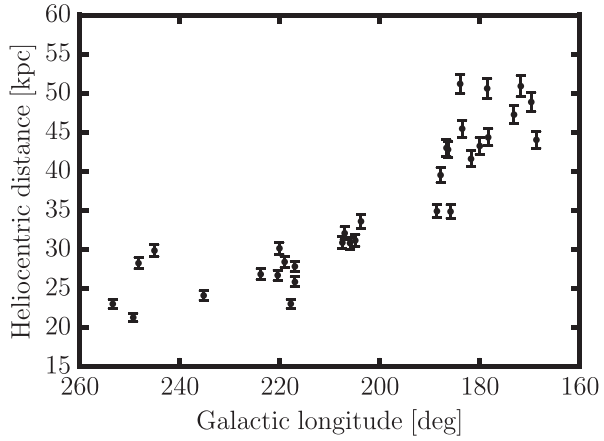

Figure 3. Measured heliocentric distances of the SMHASH Orphan RR Lyrae stars as a function of Galactic longitude. At large distances, around 50 kpc, the stream has a distance dispersion of 5 kpc. This is is much larger than its 1.6 kpc width in the plane of the sky.

large distances. Near $l = 184°$, the stream contains stars separated by 16 kpc in heliocentric distance, and the stars at $l < 195°$ have a dispersion of 5 kpc, dramatically deeper than the ∼1.6 kpc width calculated from the on-sky FWHM. In Section 6, we will argue that this depth contains information about the stream's progenitor. Overall, the SMHASH distances are in good agreement (∼1σ) with the previous work of Sesar et al. (2013), who used an optical LZ relation (Cacciari & Clementini 2003) to obtain distances to these same RR Lyrae stars. On average we find that our measurements are 5 per cent larger than the values of Sesar et al. (2013); notably, however, we find that their two most remote stars are ∼5 kpc closer, reducing the maximum heliocentric distance of the stream from about 55 to about 51 kpc.

4 PROPERTIES OF THE ORPHAN STREAM

In the following, we assume that all of the SMHASH RR Lyrae stars do indeed belong to the Orphan Stream, and so use them to outline its path and properties. We do this by (i) assuming a form for a galactic potential; (ii) finding the parameters of the potential and the orbit within that potential that best fits the centroid of the RRL positions in their measured dimensions; and (iii) measuring the dispersions in line-of-sight distance, angular size on the sky, and radial velocity about this best-fitting orbit.

Note that, since orbits of debris stars are offset from the progenitor satellite orbit (Johnston 1998; Helmi & White 1999), we expect this approach to provide *biased* estimates of the true potential parameters and orbit of the progenitor (see Eyre & Binney 2011; Sanders & Binney 2013; Lux et al. 2013, as well as our own exploration in Section 5.2). We nevertheless choose to fit orbits and potentials rather than – for example – a polynomial to the path since this allows us to both measure the structure of the stream via its depth and compare our results to the prior work of Newberg et al. (2010). The reader is cautioned that the 'best–fitting' potential and orbit are not expected to correspond exactly to the potential of the Milky Way or the orbit of the progenitor. However, the dispersion about the path outlined by the stream *do* contain clues to the nature of the progenitor (see Section 6).

4.1 Fitting method

To fit an orbit to our RRL, we use `emcee` (Foreman-Mackey et al. 2013), a Python implementation of an affine-invariant ensemble sampler for a Markov Chain Monte Carlo (MCMC) algorithm (Goodman & Weare 2010), to draw samples from the posterior probability density of the model parameters. This method is similar to that of Koposov et al. (2010), Sesar et al. (2015), and Price-Whelan et al. (2016).

4.1.1 Potential model

The Milky Way potential is represented as three smooth, static components: a Miyamoto & Nagai (1975) disk, a Hernquist (Hernquist 1990) bulge, and a spherical logarithmic halo, defined as

$$\Phi_{\rm disk} = -\alpha \frac{GM_{\rm disk}}{\sqrt{R^2 + (a + \sqrt{z^2 + b^2})^2}} \tag{3}$$

$$\Phi_{\rm sphere} = \frac{GM_{\rm sphere}}{r + c} \tag{4}$$

$$\Phi_{\rm halo} = v_{\rm halo}^2 \ln\left(R^2 + z^2 + r_h^2\right) \tag{5}$$

with component masses $M_{\rm sphere} = 3.4 \times 10^{10} {\rm M}_\odot$ and $M_{\rm disk} = 1 \times 10^{11} {\rm M}_\odot$, disk scale length $a = 6.5$ kpc, disk scale height $b = 0.26$ kpc, bulge core radius $c = 0.7$ kpc, and halo scale radius $r_h = 12$ kpc; R and z are the cylindrical coordinates and r is the spherical radius. We fix the solar distance to the Galactic centre as $R_0 = 8$ kpc (consistent with previous work, but also measurements, e.g. Gillessen et al. 2009) and the peculiar velocity of the Sun $({\rm U,V,W})_\odot = (11.1, 12.24, 7.25)$ km s^{-1} (Schönrich, Binney & Dehnen 2010). In the orbit fitting algorithm, the only potential parameter allowed to vary is the dark matter halo's scale velocity $v_{\rm halo}$, with r_h chosen such that the total potential's circular velocity at the solar position is 220 km s^{-1} (e.g. Bovy et al. 2012). These parameters are chosen to match Model 5 of Newberg et al. (2010) (their best-fitting model with a logarithmic halo) which in turn is an implementation of the best-fitting spherical model of Law et al. (2005) except that the halo scale velocity is allowed to vary. We note that the constraint on the circular velocity precludes us from fitting precisely Newberg et al.

(2010)'s Model 5 since that potential's circular velocity at the solar position is only 207 km s^{-1}.

4.2 Model parameters

We wish to find the phase space coordinates of the initial condition $\mathbf{x}^0 = (l,\ b,\ \mathrm{DM},\ \mu_l,\ \mu_b,\ v_r)^0$ for the orbit that best reproduces the observed sky positions l_i, b_i, heliocentric radial velocities $v_{r,i}$ and distance modulii DM_i of the RRL given their uncertainties $\sigma_{v_{r,i}}, \sigma_{\mathrm{DM}_i}$. The sky coordinates are assumed perfectly known and are transformed to the Orphan frame Λ, B defined in Newberg et al. (2010), a heliocentric spherical coordinate system in which the Orphan Stream lies approximately on the equator. The rotation between Galactic coordinates and the Orphan coordinates is defined by the Euler angles $(\phi, \theta, \psi) = (128.79^\circ, 54.39^\circ, 90.70^\circ)$. We set $l^0 = 200^\circ$ without interesting loss of generality.

Because tidal streams are generated with orbital parameters somewhat offset from the progenitor galaxy and with some intrinsic scatter (cf. Hendel & Johnston 2015, and references therein) we also include additional model parameters $\delta = (\delta_B, \delta_{v_r}, \delta_{DM})$ to account for the average dispersions in the observational coordinates. We neglect the fact that each of these dispersions will vary along the stream. Besides representing the physical width, velocity dispersion, and depth of the stream, they serve to deter overfitting in coordinates where δ/σ is large. The last parameter is the halo scale velocity v_{halo}. The full parameter set is then $\theta = ((b,\ DM,\ \mu_l,\ \mu_b,\ v_r)^0, (\delta_B, \delta_{v_r}, \delta_{DM}), v_{\mathrm{halo}})$. Orbits were integrated using a symplectic leapfrog integrator as implemented in the Gala package (Price-Whelan 2017).

The MCMC algorithm uses 144 walkers to explore this nine-dimensional parameter space. After running for a burn-in period of 1 000 steps, the sampler is restarted and run for an additional 10 000 steps. Since the autocorrelation time for each walker is ∼50 steps in all dimensions, only every 100th sample is taken from the chains to be included in the posterior. This ensures that each is a nearly independent sample from the posterior distribution. The autocorrelation time does not change substantially after the burn-in period, indicating that the sampling has converged.

4.2.1 Likelihood

We assume that our data are independent and that the uncertainties in each coordinate are normally distributed. Thus, the joint likelihood is the product of the likelihoods in each coordinate, which are

$$p(B_i|\Lambda_i, \theta) = \mathcal{N}(B_i|B^{\mathrm{model}}(\Lambda_i), \delta_B^2) \tag{6}$$

$$p(v_{r_i}|\Lambda_i, \theta) = \mathcal{N}(v_{r_i}|v_r^{\mathrm{model}}(\Lambda_i), \sigma_{v_r}^2 + \delta_{v_r}^2) \tag{7}$$

$$p(DM_i|\Lambda_i, \theta) = \mathcal{N}(DM_i|DM^{\mathrm{model}}(\Lambda_i), \sigma_{DM}^2 + \delta_{DM}^2), \tag{8}$$

where B^{model}, v_r^{model}, and $\mathrm{DM}^{\mathrm{model}}$ are interpolated from the model orbit integrated using the initial conditions in θ and $\mathcal{N}$ is the normal distribution

$$\mathcal{N}(x|\mu, \sigma^2) = \frac{1}{\sqrt{2\pi\sigma^2}} \exp -\frac{(x-\mu)^2}{2\sigma^2} \tag{9}$$

with μ as its mean and σ its standard deviation.

4.2.2 Priors

We implement priors on Galactic latitude and distance modulus that are uniform in Cartesian space; for the former this is uniform in $\cos(b)$, while the latter is

$$p(\mathrm{DM}) \propto 10^{\frac{3}{5}\mathrm{DM}+2}. \tag{10}$$

Using the notation $\mathcal{U}(f, g)$ for the uniform distribution with endpoints f and g, we place an uninformative prior on Heliocentric radial velocity as

$$p(v_r) = \mathcal{U}(50, 300)\ \mathrm{km\ s^{-1}}. \tag{11}$$

The dispersions δ_i are required to be positive to prevent a physically equivalent but bimodal posterior that hampers the walkers' convergence. We use logarithmic (scale-invariant) priors for these parameters,

$$p(\delta_i) \propto \delta_i^{-1}. \tag{12}$$

The halo scale velocity v_{halo} must be greater than about 68 km s^{-1} to maintain a circular speed at the solar radius of 220 km s^{-1} given our choices for the other parameters. It is therefore constrained by

$$p(v_{\mathrm{halo}}) = \mathcal{U}(68, 200)\ \mathrm{km\ s^{-1}}. \tag{13}$$

Finally, we consider the two phase space dimensions that are unobserved for individual RRL: their proper motions. Since we cannot compare them to a prior on a star-by-star basis, we instead use the value for the model orbit where it crosses $l = 199.779\ 6^\circ$. This position is specifically chosen to correspond to the location of *Hubble Space Telescope* – based proper motions of Orphan Stream stars (Sohn et al. 2016). We consider two cases: first wide, uninformative priors

$$p(\mu_l\ \cos b) = \mathcal{U}(-5, 5)\ \mathrm{mas\ yr^{-1}} \tag{14}$$

$$p(\mu_b) = \mathcal{U}(-5, 5)\ \mathrm{mas\ yr^{-1}}, \tag{15}$$

and then those based on the *Hubble* observations

$$p(\mu_l\ \cos b) = \mathcal{N}(0.211, 0.05^2)\ \mathrm{mas\ yr^{-1}} \tag{16}$$

$$p(\mu_b) = \mathcal{N}(-0.774, 0.05^2)\ \mathrm{mas\ yr^{-1}}. \tag{17}$$

In the following, we will refer to the former as 'without' a proper motion prior for conciseness.

4.3 Centroid of the Orphan Stream

Fig. 4 shows a corner plot displaying projections of the orbit fitting's posterior distribution, in the case of the uniform proper motion priors. The median value of the samples in each parameter, along with uncertainties computed as the 16th and 84th percentiles (the 68 per cent credible interval), are summarized in Table 2. We confirm that the orbit is prograde with respect to the Milky Way's rotation. Even if the walkers are restricted to only exploring the space of retrograde orbits, there are no local maxima to compare to the prograde fit shown here. If the overdensity detected by Grillmair et al. (2015) is indeed the nearly disrupted progenitor then this direction of motion makes the SMHASH RR Lyrae stars part of the leading tidal tail. The median distance modulus of 17.68 mag corresponds to a heliocentric distance of 34.2 kpc; this is approximately 150 pc more distant than Newberg et al. (2010)'s Model 5 orbit at the same longitude, which is compatible within their respective uncertainties.

Focusing on each of the two-dimensional histograms in Fig. 4 in turn, one sees that the fit parameters have minimal covariance with few exceptions: the proper motions $\mu_l \cos(b)$ with μ_b, v_{halo} with $\mu_l \cos(b)$, and to a lesser extent v_{halo} with μ_b and with v_r. Note that

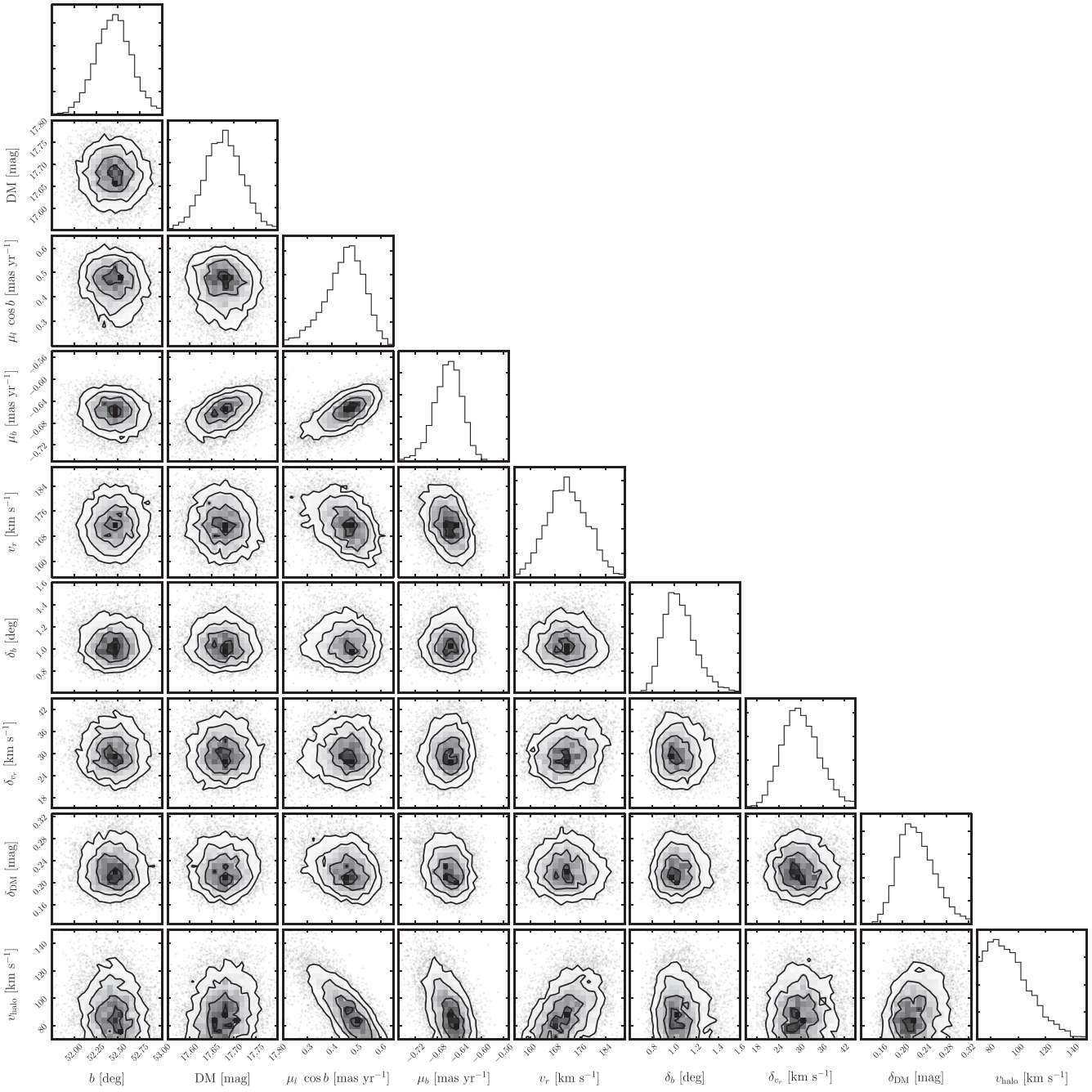

Figure 4. Corner plot (Foreman-Mackey 2016) displaying the posterior distributions of the MCMC walkers for the case of uninformative proper motion priors. Contour plots show the posterior marginalized over the other seven dimensions; histograms are marginalized over all but one. In general, there is little covariance between parameters with the notable exceptions of $\mu_l \cos b$ with μ_b and the velocity components with $v_{\rm halo}$. This suggests that precise proper motion measurements will add significantly to the constraint on enclosed mass.

the stream's Galactic latitude varies by only a few degrees in the area of our observations. It is no coincidence that the velocity components covary with the scale of the halo; this represents the need for additional kinetic energy to reach the same Galactocentric radius in a deeper potential. This means that currently available proper motion measurements can be highly informative when applied in combination with SMHASH's precision distances. For example, the 68 per cent credible interval of the marginalized posterior for $\mu_l \cos(b)$ spans almost 0.2 mas yr^{-1}, while the uncertainty on the same quantity computed from the measurement of Sohn et al. (2016) is ≈ 0.05 mas yr^{-1}.

4.4 Stream fitting with six-dimensional constraints

Fig. 5 illustrates the effect of the precise proper motion priors on the final positions of the MCMC walkers on the three most affected dimensions – $\mu_l \cos(b)$, μ_b, and $v_{\rm halo}$. On the left, we highlight these quantities in the uninformative case; here we find $\mu_l \cos(b)$ and μ_b from the best-fitting orbits are $\sim 2\sigma$ discrepant with the measured value. The strength of the Sohn et al. (2016) priors are such that when applied to the walkers (on the right) the means of the marginalized posterior distributions are shifted wholesale, making the two nearly disjoint. The halo-scale parameter is dragged to significantly higher

Table 2. Median and 68% credible intervals of parameters in the posterior distribution resulting from orbit fitting to the SMHASH data, with and without including the observational proper motion constraints. The fixed Galactic longitude value used for the initial condition is included for completeness, along with the mass enclosed at 60 kpc and circular velocities at 25, 40, and 60 kpc implied by the $v_{\rm halo}$ distribution.

Parameter	Without PM prior	With PM prior
l (deg)	199.779 6	199.779 6
b (deg)	$52.45^{+0.21}_{-0.21}$	$52.46^{+0.23}_{-0.21}$
DM(mag)	$17.68^{+0.04}_{-0.04}$	$17.66^{+0.05}_{-0.05}$
μ_l cos(b) (mas yr^{-1})	$0.456^{+0.071}_{-0.096}$	$0.244^{+0.049}_{-0.051}$
μ_b (mas yr^{-1})	$-0.660^{+0.023}_{-0.028}$	$-0.715^{+0.022}_{-0.024}$
v_r (km s^{-1})	$171.7^{+6.9}_{-6.3}$	$176.2^{+6.5}_{-6.8}$
δ_B (deg)	$1.042^{+0.168}_{-0.129}$	$1.039^{+0.175}_{-0.129}$
δ_{v_r} (km s^{-1})	$29.86^{+5.72}_{-4.82}$	$29.61^{+5.81}_{-4.94}$
$\delta_{\rm DM}$ (mag)	$0.224^{+0.040}_{-0.030}$	$0.258^{+0.046}_{-0.036}$
$v_{\rm halo}$ (km s^{-1})	92^{+19}_{-14}	128^{+16}_{-17}
M(60 kpc) (10^{11} M$_\odot$)	$3.4^{+1.1}_{-0.65}$	$5.6^{+1.2}_{-1.1}$
$v_{\rm circ}$(25 kpc) (km s^{-1})	191^{+14}_{-10}	216^{+10}_{-11}
$v_{\rm circ}$(40 kpc) (km s^{-1})	173^{+19}_{-13}	208^{+15}_{-16}
$v_{\rm circ}$(60 kpc) (km s^{-1})	161^{+21}_{-15}	202^{+18}_{-19}

values, as one would naively expect based on the covariance with $\mu_l \cos(b)$.

The marginalized posterior of $v_{\rm halo}$ can be directly converted into a distribution of enclosed masses at any given radius; we choose 60 kpc for convenient comparison with literature values. The results of this transformation are shown in Fig. 6, both without (in blue hatch) and with (in red) the *HST* proper motions as a prior.[3] The difference between them is substantial: the latter's median value is 64 per cent larger than the former; however, due to the large confidence intervals they are consistent at the $\sim 1.4\sigma$ level. The apparent narrowness of the blue posterior distribution is driven by the assumption that the circular speed at the Solar radius is 220 km s^{-1}. Given our model, this requires a minimum total mass of $\sim 2.4 \times 10^{11}$ M$_\odot$ at 60 kpc. To facilitate comparison with observations and other methods that use different potential shapes, we have also tabulated circular velocities at 25, 40, and 60 kpc in Table 2. For example, Watkins et al. (2018) recently used *Gaia* and *HST* proper motions of halo globular clusters to obtain $v_{\rm circ}(39.5\ {\rm kpc}) = 220^{+17}_{-16}$ km s^{-1}, which agrees well with our results when applying the the *HST* proper motion prior.

A selection of orbits generated from randomly chosen samples of the posteriors are shown in Fig. 7. The left-hand (right-hand) panels show the results without (with) including informative proper motion priors. Plotted from top to bottom are projections in the three observational coordinates (Galactic latitude, radial velocity, and distance) as a function of Galactic longitude. Both sets of samples capture the path of the stream over most of the survey area. Individual orbits diverge somewhat around $l \lesssim 170^\circ$, where the depth in line-of-sight distance is large. Both sets of orbits seem to systematically overestimate the Heliocentric radial velocity of stars above $l \approx 250^\circ$, however individual stars are only offset by $\sim 1\,\delta_i$. Including the Sohn et al. (2016) measurement slightly improves the match to the data in b and v_r but causes the distance to the far end of the stream to be underestimated. This is problematic because the leading arm of the stream is made up of stars with lower specific energy than the progenitor and are expected to be *interior* to its orbit. We interpret this mismatch as evidence that the 1-parameter potential model used here is not flexible enough to recover the full phase space structure of the stream. In the *N*–body models described below, there is no offset between fitted orbits and selected particles at the 0.05 mas yr^{-1} level.

[3]The Sohn et al. (2016) measurement is error-weighted; using the average motion instead both increases the uncertainty and shifts the mean towards the values found using the uniform prior, resulting in a posterior with intermediate values of $v_{\rm halo} = 112^{+18}_{-17}$ km s^{-1} and M(60 kpc) $= 4.6^{+1.0}_{-1.2} \times 10^{11}$ M$_\odot$.

4.5 The solar circular velocity as measured from the Orphan Stream

To the extent that a stream follows an orbit, the proper motion of member stars perpendicular to the stream should be zero. Any observed perpendicular proper motion is therefore a measure of the solar reflex (c.f. Carlin et al. 2012). The *Hubble* proper motion measurement and the SMHASH distance distribution posterior can be combined at the longitude of the Sohn et al. (2016) Orphan F1 field to estimate the solar motion.

We define a new coordinates system relative to the Orphan coordinates of Newberg et al. (2010) with axes that point into the plane of the sky, parallel to the stream, and perpendicular to the stream. The unit vector perpendicular to the stream points in the direction (in Orphan coordinates) $\hat{n} = (0.62619,\ 0.50664,\ 0.59261)$. In this direction, the marginalized posterior derived using the *Hubble* proper motion priors approximates a Gaussian with mean 136.5 km s^{-1} and dispersion 9.1 km s^{-1}. If we assume that the solar peculiar velocity relative to the local standard of rest (LSR) is known from Schönrich et al. (2010), then this implies that the azimuthal velocity of the LSR (which equals the circular velocity if the disk is circular) is $v_y = 235 \pm 16$ km s^{-1}. This result is consistent with both the traditional IAU value of 220 km s^{-1} as well as more recent studies that give somewhat larger results (e.g. McMillan 2011; Bovy et al. 2012). While this new measurement does not help to resolve the controversy surrounding the exact value of the solar motion, it does provide an independent consistency check on the SMHASH distances.

5 IMPLICATIONS FOR THE MILKY WAY'S MASS

Orbit fitting is known to introduce systematic biases in potential measures (Eyre & Binney 2011; Lux et al. 2013; Sanders & Binney 2013). To investigate what effect this might have for the specific case of the Orphan Stream, we have created *N*–body models of the stream and 'observed' them in such a way as to recreate the SMHASH dataset. We then apply an identical orbit fitting technique and compare with the simulation inputs. This method allows us to contextualize the results of our RRL observations in terms of the direction and size of systematic biases as well as compare them with earlier results.

Previous measurements of the Milky Way's mass using the Orphan Stream found that the best-fitting halo was a factor of ~ 2 less massive inside 60 kpc (2.74×10^{11} M$_\odot$; Newberg et al. 2010) than contemporary models using other techniques, such as fitting Sagittarius Stream data (4.7×10^{11} M$_\odot$; Law et al. 2005) or the velocity distribution of field BHB stars (4.0×10^{11} M$_\odot$; Xue et al. 2008). A complete summary of mass estimates is outside the scope of this work; the review of Bland-Hawthorn & Gerhard (2016) provides an overview. However, the Newberg et al. (2010) measurement remains below all other published estimates, with recent results

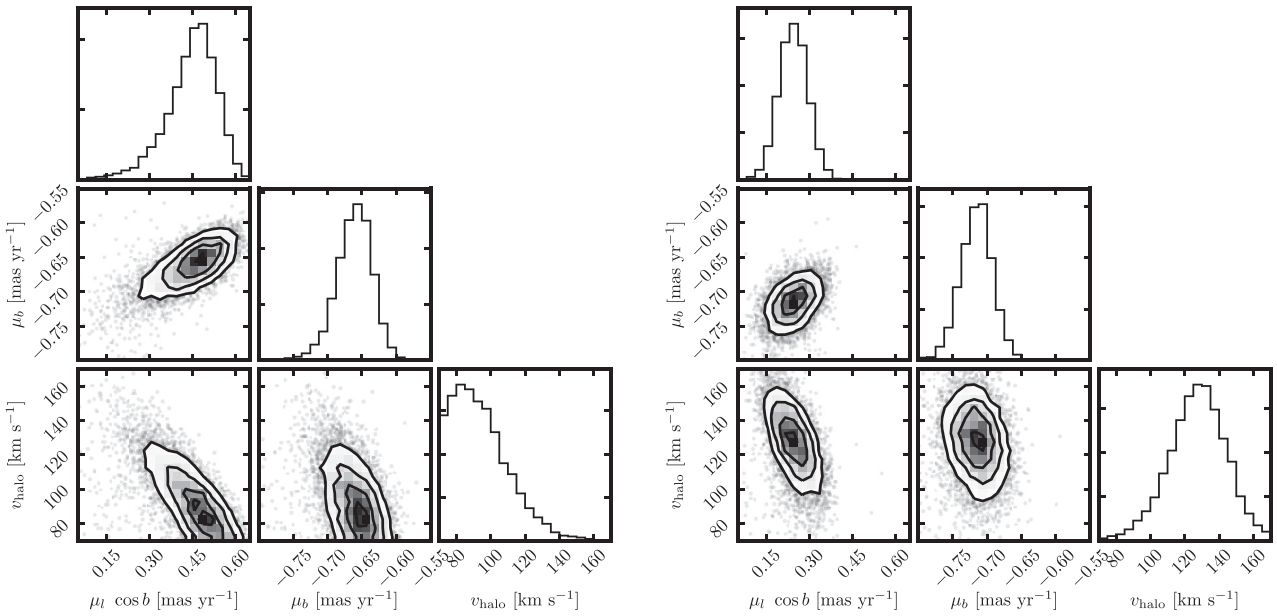

Figure 5. Corner plot displaying the marginalized posterior distributions for the model parameters $\mu_l \cos(b)$, μ_b, and $v_{\rm halo}$ along with their covariances. Left: uniform prior on $\mu_l \cos(b)$ and μ_b. Right: result when otherwise identical chains are run with the additional priors $p(\mu_l \cos(b)) = \mathcal{N}(0.211, 0.05^2)$, $p(\mu_b) = \mathcal{N}(-0.774, 0.05^2)$. Due to the covariance between the proper motions and the halo-scale velocity, these priors result in a median $v_{\rm halo}$ that corresponds to a halo 64 per cent more massive than the uniform case.

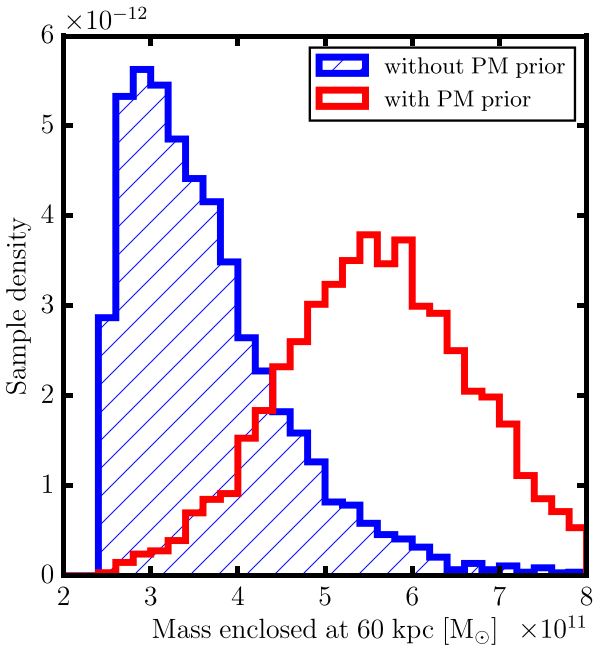

Figure 6. Milky Way mass enclosed at 60 kpc, calculated from the scale velocities $v_{\rm halo}$ of the samples. Including the proper motion prior noticeably increases the median value, from $3.4 \times 10^{11}\,{\rm M}_\odot$ (in blue hatch) to $5.6 \times 10^{11}{\rm M}_\odot$ (in red), but the confidence intervals are consistent at $\sim 1.4\sigma$.

reaching masses only as low as about $3.2 \times 10^{11}\,{\rm M}_\odot$ (Gibbons et al. 2014).

5.1 Creating and observing mock data sets

We use the self-consistent field method (SCF; Hernquist & Ostriker 1992), which represents the gravitational potential of the disrupting satellite as a basis function expansion, to create a series of *N*-body simulations designed to reasonably mimic the observed Orphan Stream. The single-component, dark matter only Orphan progenitor is implemented as a Navarro–Frenk–White (NFW; Navarro, Frenk & White 1997) distribution with 10^5 particles. The particles are instantiated out to 35 scale radii and so the model's total mass differs from the virial mass; in the following we report the corresponding virial mass to avoid confusion. All simulations have the same mean density inside the scale radius, which results in tides unbinding them at approximately the same time. This allows the separation of effects due to the time of disruption and passive evolution. The density scaling is set such that the halo with a virial mass of $10^9\,{\rm M}_\odot$ has a scale radius of 0.75 kpc although the results are not particularly sensitive to this choice.

We chose the orbit and potential model to be precisely that of Newberg et al. (2010)'s Model 5: that is, an orbit initialized from the phase space coordinate with Heliocentric position $(l, b, R) = (218^\circ, 53.5^\circ, 28.6\,{\rm kpc})$ and Galactocentric velocity $(v_x, v_y, v_z) = (-156, 79, 107)\,{\rm km\,s^{-1}}$ moving in a logarithmic potential model (equations 3–5) with the one unspecified parameter $v_{\rm halo}$ set to $73\,{\rm km\,s^{-1}}$. The orbit is integrated backwards in time to find the phase space coordinate of the third apocenter, 4.8 Gyr ago. When the satellite is near apocenter the hosts' tidal field is at its weakest, so beginning the simulation here minimizes artificial gravitational shocking. After relaxing in isolation the host potential is turned on over 10 internal dynamical times, the particle distribution is inserted, and the satellite is evolved to the present day. We assume that the current position of the progenitor is at the overdensity identified by Grillmair et al. (2015), $l \approx 268.7^\circ$, so the simulation ends at that point.

To produce synthetic observations that approximate those of the SMHASH RRL, we first select the particles below the tenth percentile in initial internal binding energy. These are tagged as stars. This simple strategy has been shown to reproduce the observed properties of Local Group dwarf galaxies in semianalytic models

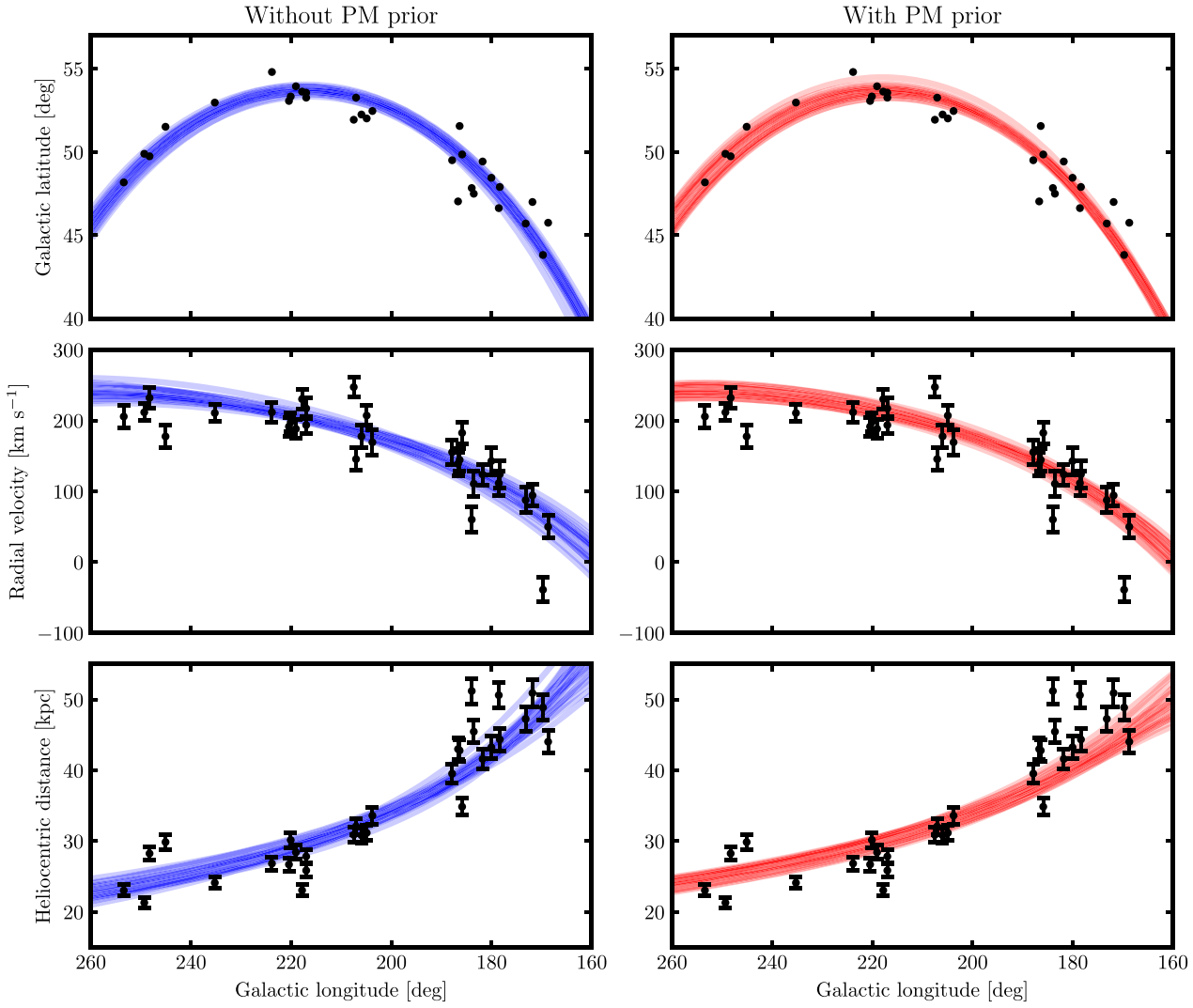

Figure 7. Left: a selection of orbit fits (blue lines) generated from randomly selected samples of the posterior distribution shown in Fig. 4, where the proper motion prior is uninformative. Right: the same (red lines), but with samples from the walkers constrained by the observed $\mu_l \cos b$ and μ_b. The former better reproduces the trend of distance with longitude, while the latter slightly improves the match in radial velocity and sky position, especially at $l > 240°$.

(Bullock & Johnston 2005) and create stellar haloes with realistic properties in simulations of Milky Way-like galaxies with cosmological infall (De Lucia & Helmi 2008; Cooper et al. 2010). From this subset, we choose at random 30 particles that match the selection criteria used in Sesar et al. (2013), namely Galactic longitude $260° > l > 160°$, Orphan latitude $4° > B > -4°$, and Galactic standard of rest velocity $v_{gsr} > 40\,\mathrm{km\,s^{-1}}$. Since the particle positions and velocities are precisely known, we introduce 'observational' uncertainties by adding a random velocity drawn from a Gaussian of width $15\,\mathrm{km\,s^{-1}}$ to each particle's heliocentric velocity. Similarly, the selected particles are scattered in heliocentric distance according to the 2.5 per cent relative uncertainty demonstrated in Fig. 2. These same values are retained as uncertainties to be fed into the orbit fitting algorithm as well.

5.2 Biases in orbit fitting

The problems associated with assuming stars in a tidal stream follow a single orbit are conceptually simplified when considering the Orphan Stream since we observe only the leading tail. In this case, stars farther from the satellite – towards apocenter – have lower total energy than the progenitor, with the difference tending to increase with distance; their individual orbits turn around at smaller Galactocentric radii than the progenitor's does. Thus, orbits matched to the stream's path are tracing both the loss of kinetic energy to the gravitational potential as well as an additional loss determined by the total energy gradient of stars along the stream. Since the latter is not modelled in orbit fitting, the potential needs to be deeper at fixed radius to compensate for this 'extra' loss, leading to an inflated mass estimate.

Fig. 8 illustrates the typical systematic errors in inferred mass introduced by this effect. Despite the fact that each simulation was run in a potential with $M_{\rm encl}(60\,\mathrm{kpc}) = 2.7 \times 10^{11}\,\mathrm{M}_\odot$, the median value of the marginalized posterior distributions of $v_{\rm halo}$ generate an estimate $\sim$ 20–50 per cent more massive. There is also an additional realization-dependent scatter of order 20 per cent, not depicted here. The bias is nearly independent of satellite mass, which matches theoretical expectations (Sanders & Binney 2013). To our knowledge this is the first time that the bias in mass enclosed due to orbit fitting has been quantified in a scenario that replicates an observed system. The magnitude of the effect presumably depends on the details of

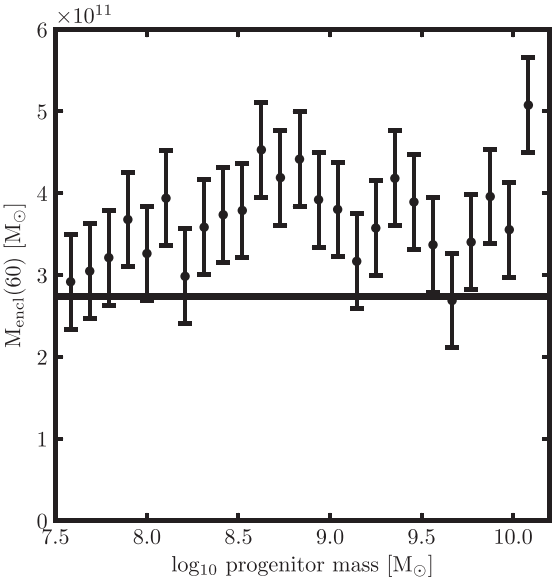

Figure 8. Bias in the best-fitting host halo's enclosed mass, calculated from $v_{\rm halo}$, as a function of the initial halo mass of the progenitor satellite. The black horizontal line represents the true value in the model potential, while the points illustrate the transformed posterior distribution. The median value exceeds expectations by typically 20–50 per cent.

the potential model but the direction should not – the fitting algorithm will tend to prefer haloes that are more massive than are correct. In fact, the synthetic data that produce the correct answer seem to be less representative of the underlying simulation, in terms of their on-sky and distance distributions, than those that produce biased results. For this reason, we report the mass value measured for the Milky Way only as an upper limit.

We also note that the already low enclosed mass measurement of Newberg et al. (2010)'s Model 5 should also be affected by this systematic error since the approximation is the same despite their different fitting technique. If the magnitude of the bias is identical then the corrected mass enclosed is approximately $1.8 \times 10^{11}\,{\rm M}_\odot$, slightly more than half that found by Gibbons et al. (2014). Models with such small enclosed masses may have difficulty matching other observables such as the circular velocity of the Sun.

6 THE ORPHAN PROGENITOR

In the previous section, we were concerned primarily with the model parameters that describe the phase space position of the orbits and the shape of the potential. Now, we focus on the internal structure of the stream, characterized by the dispersions δ_B, δ_{v_r}, and $\delta_{\rm DM}$. For a particular progenitor orbit, the spatial and velocity scales of the stream stars vary with the satellite-to-host mass ratio as $(m/M)^{1/3}$ (Johnston 1998; Helmi & White 1999; Johnston, Sackett & Bullock 2001); therefore the δ_i contain information about the progenitor system. To first order, this is the mass when the stars are unbound; however, it may be possible to recover the satellite's central density distribution which also imprints itself on the stream (Errani, Peñarrubia & Tormen 2015).

Fig. 9 shows the effect of satellite mass on the simulated streams' structural parameters. In each panel, the horizontal blue lines illustrate the values measured from the SMHASH data while the black points show the same quantities found after applying the same orbit fitting algorithm to *N*-body simulations of varying initial satellite

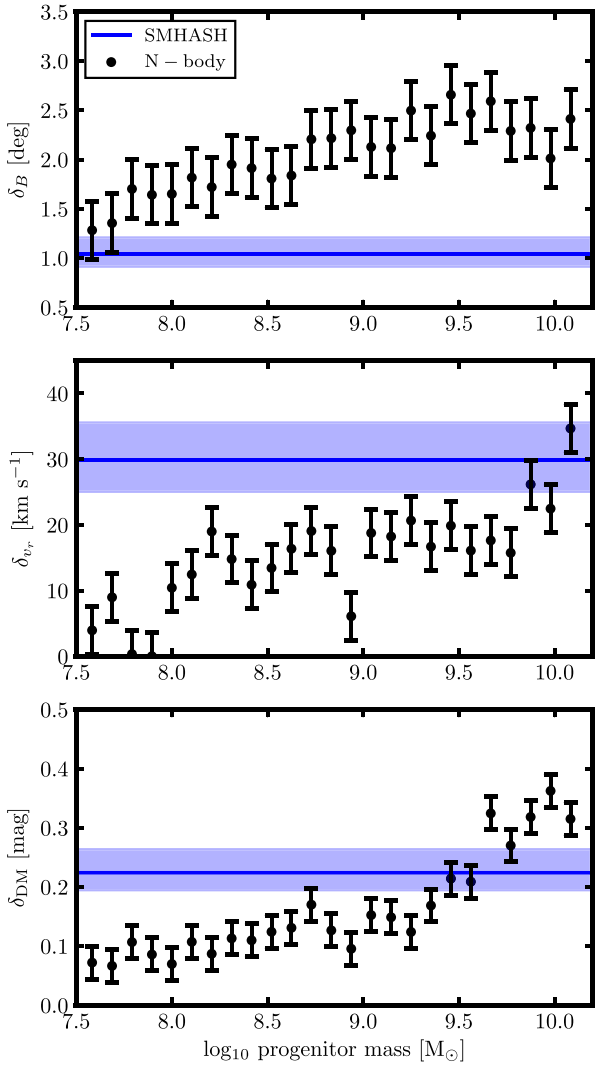

Figure 9. Fitted values of width on the sky (top), velocity dispersion (center), and line-of-sight depth (bottom) for a set of *N*-body models of the Orphan Stream (black points) as a function of model satellite mass, compared to the same quantities as measured for the SMHASH Orphan data (blue region).

halo masses. The mass range shown, from 3.8×10^7 to $1.2 \times 10^{10}\,{\rm M}_\odot$, captures dwarf galaxies from the ultrafaints to a few times less massive than the Small Magellanic Cloud (Guo et al. 2010).

First, we consider the stream's width on the sky, δ_B, plotted in the upper panel. The measured value $\delta_B = 1^\circ$ appears at a glance to be most consistent with the lowest mass simulations, indicating that $M_{\rm Orphan} \approx 10^8\,{\rm M}_\odot$. However, the selection of RR Lyrae stars for spectroscopic follow-up in the SMHASH precursor catalogues is non-uniform and appears to be weighted significantly towards stars that are nearer the stream centre (e.g. of the stars with $2^\circ < B < 4^\circ$, 3 have spectra and 11 do not). The observed δ_B is therefore unlikely to be representative of the true distribution. An alternative approach is to look at studies of Orphan's main sequence population; since our synthetic RRL are selected at random from the 'star' particles, they represent any other stellar population just as well under the assumption that Orphan was originally well mixed. Belokurov et al. (2007) found that the stream has a full-width at

half-maximum of around 2°, which is comparable to the SMHASH RRL $\delta_B = 1°$. However, Sales et al. (2008) showed that the observed stream width may be truncated by confusion with the Galactic background and that streams as wide as 15° could be hidden in the data. We therefore take δ_B as measured in SMHASH as a lower limit on acceptable values in the *N*-body simulations, indicating $M_{\rm Orphan} \gtrsim 10^8\,{\rm M}_\odot$.

Next, we consider the velocity dispersion δ_{v_r}, shown in the middle panel of Fig. 9. It is clear that our model fits cannot reproduce the observed velocity dispersion except in the case of the highest mass progenitors. In fact, the true dispersion is buried by the simulated velocity errors for the lower mass models, resulting in a flat profile across much of the mass range. To obtain the 30 km s^{-1} required to match the δ_{v_r} fit to the (Sesar et al. 2013) velocities would require a satellite of mass $\gtrsim 10^{10}\,{\rm M}_\odot$. Such a progenitor seems unlikely given Orphan's luminosity and metallicity as well as the other structural parameters. In addition, Newberg et al. (2010) measured the velocity dispersion of Orphan's BHB stars and found $\sigma_v = 8$–13 km s^{-1} at various points along the stream; similarly, the K-giants surveyed by Casey et al. (2013) have a velocity dispersion of 6.5 ± 7.0 km s^{-1}. Values in the 5–15 km s^{-1} range are consistent with a wide variety of *N*-body models. We note that obtaining systemic velocities for RRL requires subtraction of the stars' atmospheric velocities as they pulsate. The velocity variation of spectral lines over a single cycle can approach 100 km s^{-1} (e.g. Preston 2011), so if even a fraction remains it could explain this discrepancy. Due to this concerns we place lower weight on δ_{v_r} as a constraint and consider it as only an upper limit on progenitor mass.

Finally, the bottom panel of Fig. 9 shows the trend of line-of-sight depth in distance modulus, $\delta_{\rm DM}$, as a function of progenitor mass. Of our measurements this dimension provides the most confident constraint on the Orphan progenitor. A line fit to the apparently linear behaviour of the models above $10^9\,{\rm M}_\odot$ shows that an initial mass $M_{\rm Orphan} \approx 3.2 \times 10^9\,{\rm M}_\odot$ best reproduces the observed depth of 0.224 mag. At high satellite mass the stream begins fanning out near apocenter due to azimuthal precession of the orbits, leading to larger depths and increased dependence of measured parameters on the selection of simulation particles as RRL.

Taken as a whole, the structure of the stream suggests a progenitor with initial halo mass of several times $10^9\,{\rm M}_\odot$. That value is in good agreement with the Local Group dwarf spheroidals, who seem to live in haloes in this range (Peñarrubia, McConnachie & Navarro 2008; Boylan-Kolchin, Bullock & Kaplinghat 2012; Fattahi et al. 2016) and provides further evidence that Orphan is indeed a disrupted dwarf spheroidal galaxy. Satellite mass measurements obtained in this way are naturally potential-dependent since the stream structure is sensitive principally to the mass ratio. While the average $v_{\rm halo}$ fit in the *N*-body models is well matched to that of SMHASH we cannot say with confidence that the bias will be identical. Using any literature value for the Milky Way's mass will vary this result by less than a factor of 2, surely less than the systematic uncertainty in this simple method.

7 SUMMARY

This work presents *Spitzer Space Telescope* observations of 32 candidate Orphan Stream RR Lyrae stars as part of the *Spitzer* Merger History and SMHASH program. Using a theoretical PLZ relation at 3.6 μm in conjunction with archival data, we have obtained distances to individual stars with 2.5 per cent relative uncertainties, a factor of 2 better than the previous state of the art. We find that the stream extends to approximately 50 kpc in heliocentric distance within the survey footprint and have resolved its large line-of-sight depth dispersion of 5 kpc as it approaches apocenter.

Using a Markov Chain Monte Carlo orbit fitting algorithm, we find that the SMHASH data are consistent with a more massive Milky Way halo than indicated by previous work using same stream and a similar technique. By comparing with *N*-body simulations of dwarf galaxy tidal disruptions, we find that orbits fit to the available Orphan data are biased to high masses, suggesting that our measurement is an upper limit (and in good agreement with other modern methodologies). While proper motion priors seem to provide significant leverage on the Milky Way's halo, our potential model is apparently too rigid to take advantage of the full phase space information. Fully integrating six-dimensional constraints is a promising avenue for future work.

By examining the structure of the stream – namely its line-of-sight depth, velocity dispersion, and width on the sky – we find that a satellite galaxy with an initial halo mass $M_{\rm Orphan} \approx 3.2 \times 10^9\,{\rm M}_\odot$ best reproduces the SMHASH data. In combination with the integrated luminosity of the stream, this indicates that the progenitor was likely comparable to the Milky Way's eight classical dwarf spheroidals.

The SMHASH RR Lyrae star distances are fertile ground for further detailed study of the Orphan Stream. The investigations presented here represent only a first step towards understanding this surprisingly complex object. Future work, including implementing sophisticated potential measuring techniques and leveraging additional data from the *Gaia* mission and others, promises to improve our knowledge of the Milky Way and its satellite system.

ACKNOWLEDGEMENTS

DH thanks Peter Stetson, Sheila Kannappan, and Vasily Belokurov for helpful discussions and the anonymous referee for a thoughtful and constructive report. This work is based on observations made with the *Spitzer Space Telescope*, which is operated by the Jet Propulsion Laboratory, California Institute of Technology under a contract with the National Aeronautics and Space Administration (NASA). DH and KVJ acknowledge support on various aspects of this project from NASA through subcontract JPL 1558281 and ATP grant NNX15AK78G, as well as from the National Science Foundation (NSF) through the grant AST-1614743. The Space Telescope Science Institute (STScI) coauthors acknowledge NASA support through a grant for *HST* program GO-13443 from STScI, which is operated by the Association of Universities for Research in Astronomy (AURA), Inc., under NASA contract NAS5-26555. Support for this work was provided by NASA through Hubble Fellowship grant #51386.01 awarded to RLB by the Space Telescope Science Institute, which is operated by the Association of Universities for Research in Astronomy, Inc., for NASA, under contract NAS 5-26555. M-RC acknowledges support from the European Research Council (ERC) under European Union's Horizon 2020 research and innovation programme (grant agreement No. 652115). GC and AG acknowledge support from the Istituto Nazionale di Astrofisica (INAF) through PRIN-INAF2014, "EXCALIBUR'S" (P.I. G. Clementini) and by the Ministero dell'Istruzione, dell'Universita e della Ricerca (MIUR), through Premiale 2015, 'MITiC' (P.I. B. Garilli). DH acknowledges the use of the Shared Research Computing Facility at Columbia University. This work made use of Matplotlib (Hunter 2007), SciPy (Jones et al. 2001), Astropy (Astropy Collaboration et al. 2013), and the Astropy-affiliated Gala package (Price-Whelan 2017). This work has made use of data from the European Space Agency

(ESA) mission *Gaia* (https://www.cosmos.esa.int/gaia), processed by the *Gaia* Data Processing and Analysis Consortium (DPAC, https://www.cosmos.esa.int/web/gaia/dpac/consortium). Funding for the DPAC has been provided by national institutions, in particular the institutions participating in the *Gaia* Multilateral Agreement.

REFERENCES

Amorisco N. C., 2015, MNRAS, 450, 575
Arenou F. et al., 2018, A&A, preprint (arXiv:1804.09375)
Astropy Collaboration et al., 2013, A&A, 558, A33
Belokurov V. et al., 2006, ApJ, 642, L137
Belokurov V. et al., 2007, ApJ, 658, 337
Bersier D., Wood P. R., 2002, AJ, 123, 840
Bland-Hawthorn J., Gerhard O., 2016, ARA&A, 54, 529
Bono G., Caputo F., Castellani V., Marconi M., Storm J., 2001, MNRAS, 326, 1183
Bono G., Caputo F., Castellani V., Marconi M., Storm J., Degl'Innocenti S., 2003, MNRAS, 344, 1097
Bovy J. et al., 2012, ApJ, 759, 131
Bovy J., Bahmanyar A., Fritz T. K., Kallivayalil N., 2016, ApJ, 833, 31
Boylan-Kolchin M., Bullock J. S., Kaplinghat M., 2012, MNRAS, 422, 1203
Braga V. F. et al., 2015, ApJ, 799, 165
Brown W. R., Geller M. J., Kenyon S. J., Diaferio A., 2010, AJ, 139, 59
Bullock J. S., Johnston K. V., 2005, ApJ, 635, 931
Bullock J. S., Kravtsov A. V., Weinberg D. H., 2001, ApJ, 548, 33
Cacciari C., Clementini G., 2003, in Alloin D., Gieren W., eds, Lecture Notes in Physics, Vol. 635, Stellar Candles for the Extragalactic Distance Scale. Springer-Verlag, Berlin, p. 105
Cardelli J. A., Clayton G. C., Mathis J. S., 1989, ApJ, 345, 245
Carlin J. L., Majewski S. R., Casetti-Dinescu D. I., Law D. R., Girard T. M., Patterson R. J., 2012, ApJ, 744, 25
Casey A. R., Da Costa G., Keller S. C., Maunder E., 2013, ApJ, 764, 39
Catelan M., Pritzl B. J., Smith H. A., 2004, ApJS, 154, 633
Cohen J., Sesar B., Bahnolzer S., He K., Kulkarni S. R., Prince T. A., Bellm E., Laher R. R., 2017a, AJ, 849, 18
Cohen J. G., Sesar B., Bahnolzer S., He K., Kulkarni S. R., Prince T. A., Bellm E., Laher R. R., 2017b, ApJ, 849, 150
Cooper A. P. et al., 2010, MNRAS, 406, 744
De Lucia G., Helmi A., 2008, MNRAS, 391, 14
Drake A. J. et al., 2009, ApJ, 696, 870
Drake A. J. et al., 2013, ApJ, 763, 32
Errani R., Peñarrubia J., Tormen G., 2015, MNRAS, 449, L46
Eyre A., Binney J., 2011, MNRAS, 413, 1852
Fakhouri O., Ma C.-P., Boylan-Kolchin M., 2010, MNRAS, 406, 2267
Fattahi A., Navarro J. F., Sawala T., Frenk C. S., Sales L. V., Oman K., Schaller M., Wang J., 2016, MNRAS, preprint (arXiv:1607.06479)
Fazio G. G. et al., 2004, ApJS, 154, 10
Fiorentino G. et al., 2015, ApJ, 798, L12
Foreman-Mackey D., 2016, J. Open Source Soft., 24
Foreman-Mackey D., Hogg D. W., Lang D., Goodman J., 2013, PASP, 125, 306
Freedman W. L., Madore B. F., Scowcroft V., Burns C., Monson A., Persson S. E., Seibert M., Rigby J., 2012, ApJ, 758, 24
Freeman K., Bland-Hawthorn J., 2002, ARA&A, 40, 487
Fritz T. K., Kallivayalil N., 2015, ApJ, 811, 123
Gaia Collaboration Brown A. G. A., Vallenari A., Prusti T., de Bruijne J. H. J., Babusiaux C., Bailer-Jones C. A. L., 2018, A&A, preprint (arXiv:1804.09365)
Gaia Collaboration et al., 2016, A&A, 595, A1
Garofalo A., et al., 2018, MNRAS, submitted
Gibbons S. L. J., Belokurov V., Evans N. W., 2014, MNRAS, 445, 3788
Gibbons S. L. J., Belokurov V., Evans N. W., 2017, MNRAS, 464, 794
Gillessen S., Eisenhauer F., Fritz T. K., Bartko H., Dodds-Eden K., Pfuhl O., Ott T., Genzel R., 2009, ApJ, 707, L114
Goodman J., Weare J., 2010, Comm. App. Math. Comp. Sci., 5, 65
Grillmair C. J., 2006, ApJ, 645, L37
Grillmair C. J., Hetherington L., Carlberg R. G., Willman B., 2015, ApJ, 812, L26
Guo Q., White S., Li C., Boylan-Kolchin M., 2010, MNRAS, 404, 1111
Helmi A., White S. D. M., 1999, MNRAS, 307, 495
Hendel D., Johnston K. V., 2015, MNRAS, 454, 2472
Hernitschek N. et al., 2017, ApJ, 850, 96
Hernquist L., 1990, ApJ, 356, 359
Hernquist L., Ostriker J. P., 1992, ApJ, 386, 375
Hunter J. D., 2007, Comput. Sci. Eng., 9, 90
Indebetouw R. et al., 2005, ApJ, 619, 931
Johnston K. et al., 2013, SMASH: Spitzer Merger History and Shape of the Galactic Halo, Spitzer Proposal
Johnston K. V., 1998, ApJ, 495, 297
Johnston K. V., Hernquist L., Bolte M., 1996, ApJ, 465, 278
Johnston K. V., Sackett P. D., Bullock J. S., 2001, ApJ, 557, 137
Johnston K. V., Bullock J. S., Sharma S., Font A., Robertson B. E., Leitner S. N., 2008, ApJ, 689, 936
Jones E., et al., 2001, SciPy: Open source scientific tools for Python, available at: http://www.scipy.org/
Keller S. C., Murphy S., Prior S., DaCosta G., Schmidt B., 2008, ApJ, 678, 851
Kirby E. N., Cohen J. G., Guhathakurta P., Cheng L., Bullock J. S., Gallazzi A., 2013, ApJ, 779, 102
Koposov S. E. et al., 2012, ApJ, 750, 80
Koposov S. E., Rix H.-W., Hogg D. W., 2010, ApJ, 712, 260
Küpper A. H. W., Balbinot E., Bonaca A., Johnston K. V., Hogg D. W., Kroupa P., Santiago B. X., 2015, ApJ, 803, 80
Law N. M. et al., 2009, PASP, 121, 1395
Law D. R., Majewski S. R., 2010, ApJ, 714, 229
Law D. R., Johnston K. V., Majewski S. R., 2005, ApJ, 619, 807
Layden A. C., 1994, AJ, 108, 1016
Lindegren L. et al., 2018, A&A, preprint (arXiv:1804.09366)
Longmore A. J., Fernley J. A., Jameson R. F., 1986, MNRAS, 220, 279
Lux H., Read J. I., Lake G., Johnston K. V., 2013, MNRAS, 436, 2386
Madore B. F. et al., 2013, ApJ, 776, 135
Majewski S. R., Skrutskie M. F., Weinberg M. D., Ostheimer J. C., 2003, ApJ, 599, 1082
Makovoz D., Khan I., 2005, in Shopbell P., Britton M., Ebert R., eds, ASP Conf. Ser. Vol. 347: Astronomical Data Analysis Software and Systems XIV. Astron. Soc. Pac., San Francisco, p. 81
McMillan P. J., 2011, MNRAS, 414, 2446
Miyamoto M., Nagai R., 1975, PASJ, 27, 533
Muraveva T. et al., 2018, MNRAS, 473, 3131
Navarro J. F., Frenk C. S., White S. D. M., 1997, ApJ, 490, 493
Neeley J. R. et al., 2015, ApJ, 808, 11
Neeley J. R. et al., 2017, ApJ, 841, 84
Newberg H. J., Willett B. A., Yanny B., Xu Y., 2010, ApJ, 711, 32
Pawlowski M. S., Pflamm-Altenburg J., Kroupa P., 2012, MNRAS, 423, 1109
Pearson S., Küpper A. H. W., Johnston K. V., Price-Whelan A. M., 2015, ApJ, 799, 28
Peñarrubia J., McConnachie A. W., Navarro J. F., 2008, ApJ, 672, 904
Persson S. E., Madore B. F., Krzemiński W., Freedman W. L., Roth M., Murphy D. C., 2004, AJ, 128, 2239
Preston G. W., 2011, AJ, 141, 6
Price-Whelan A. M., 2017, J. Open Source Softw., 1, 24
Price-Whelan A. M., Sesar B., Johnston K. V., Rix H.-W., 2016, ApJ, 824, 104
Rau A. et al., 2009, PASP, 121, 1334
Saha A., 1985, ApJ, 289, 310
Sales L. V. et al., 2008, MNRAS, 389, 1391
Sanders J. L., Binney J., 2013, MNRAS, 433, 1813
Sanderson R. E., 2016, ApJ, 818, 41

Sanderson R. E., Helmi A., Hogg D. W., 2015, ApJ, 801, 98
Schlafly E. F., Finkbeiner D. P., 2011, ApJ, 737, 103
Schönrich R., Binney J., Dehnen W., 2010, MNRAS, 403, 1829
Scowcroft V., Freedman W. L., Madore B. F., Monson A. J., Persson S. E., Seibert M., Rigby J. R., Sturch L., 2011, ApJ, 743, 76
Sesar B. et al., 2010, ApJ, 708, 717
Sesar B. et al., 2013, ApJ, 776, 26
Sesar B. et al., 2015, ApJ, 809, 59
Sesar B., Hernitschek N., Dierickx M. I. P., Fardal M. A., Rix H.-W., 2017, ApJ, 844, L4
Sohn S. T. et al., 2016, ApJ, 833, 235
Stetson P. B., 1987, PASP, 99, 191
Stetson P. B., 1994, PASP, 106, 250
Stokes G. H., Evans J. B., Viggh H. E. M., Shelly F. C., Pearce E. C., 2000, Icarus, 148, 21
Watkins L. L. et al., 2009, MNRAS, 398, 1757
Watkins L. L., van der Marel R. P., Sohn S. T., Evans N. W., 2018, AAS, preprint (arXiv:1804.11348)
Werner M. W. et al., 2004, ApJS, 154, 1
White S. D. M., Rees M. J., 1978, MNRAS, 183, 341
Wilhelm R., Beers T. C., Sommer-Larsen J., Pier J. R., Layden A. C., Flynn C., Rossi S., Christensen P. R., 1999, AJ, 117, 2329
Xue X. X. et al., 2008, ApJ, 684, 1143
Zinn R., West M. J., 1984, ApJS, 55, 45

SUPPORTING INFORMATION

Supplementary data are available at *MNRAS* online.
smhash_orphan_epochs.txt
smhash_orphan_rrly.txt

Please note: Oxford University Press is not responsible for the content or functionality of any supporting materials supplied by the authors. Any queries (other than missing material) should be directed to the corresponding author for the article.

APPENDIX A: SMHASH LIGHT CURVES

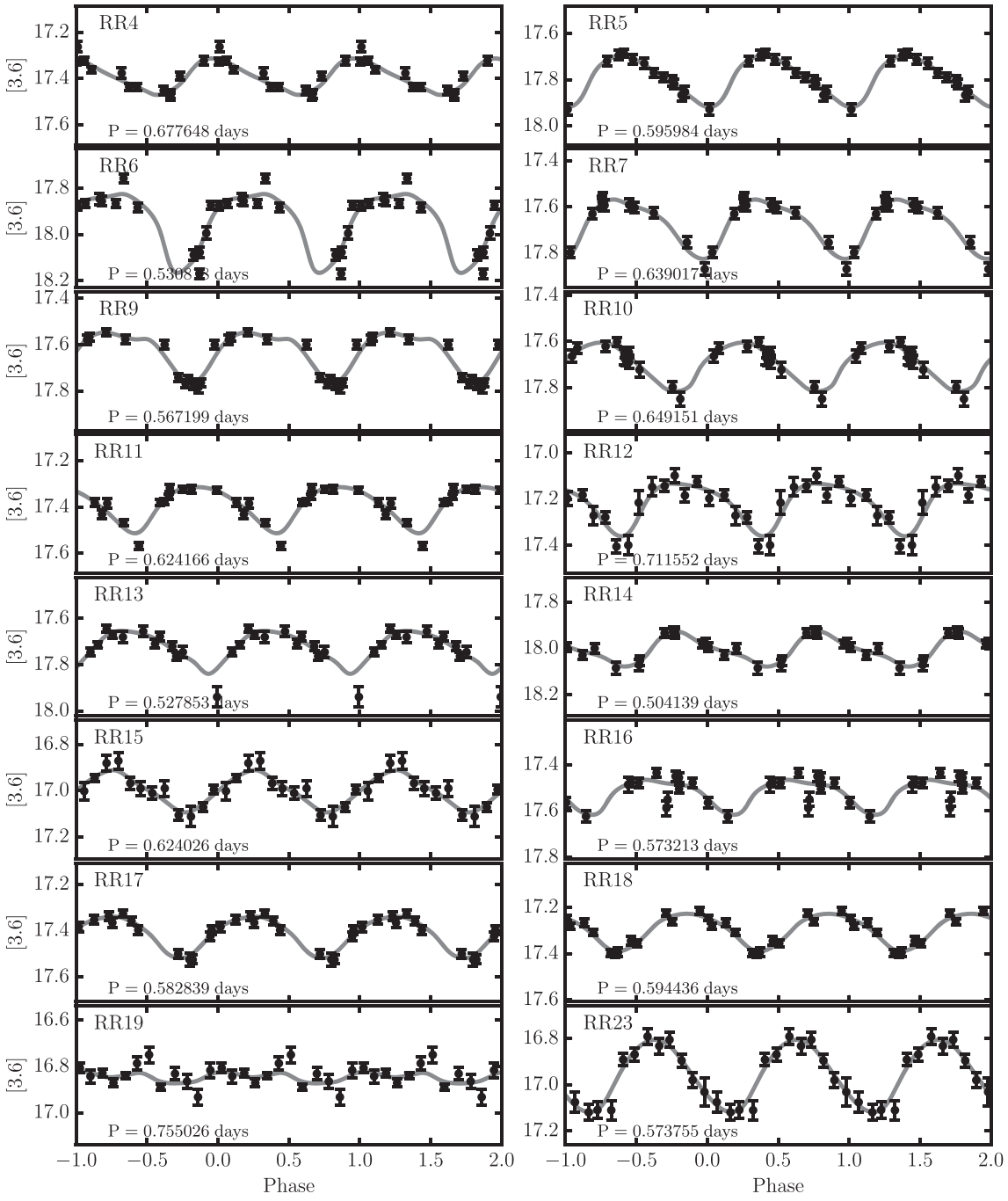

Figure A1. 2*Spitzer* 3.6 μm light curves of the 32 SMHASH Orphan Stream RR Lyrae star candidates. Each was observed in 12 epochs; the data and fitted light curves are repeated through three phase cycles for visual clarity. All stars are shown on the same scale so that amplitude variation is visible. The periods shown were measured from the archival optical survey data (Sesar et al. 2013). RR19 is likely not an RR Lyrae star or a stream member but we include it here for completeness.

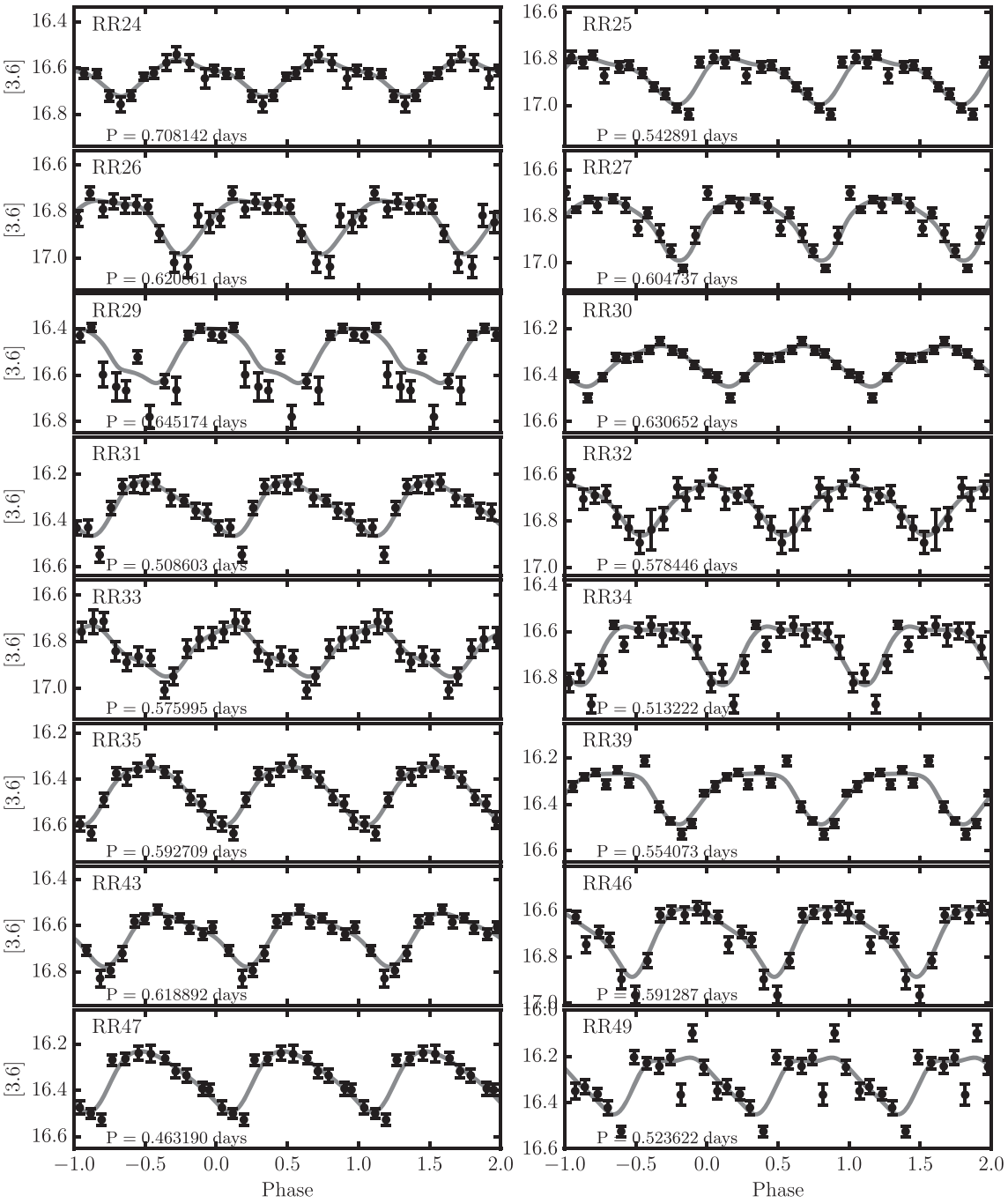

Figure A1. continued

[1]*Department of Astronomy, Columbia University, 550 West 120th Street, New York, NY 10027, USA*
[2]*Department of Physics, University of Bath, Claverton Down, Bath, BA2 7AY, UK*
[3]*Observatories of the Carnegie Institution of Washington, 813 Santa Barbara St., Pasadena, CA 91101, USA*
[4]*Space Telescope Science Institute, 3700 San Martin Drive, Baltimore, MD 21218, USA*
[5]*Center for Astrophysical Sciences, Department of Physics & Astronomy, Johns Hopkins University, Baltimore, MD 21218, USA*
[6]*Department of Astrophysical Sciences, Princeton University, 4 Ivy Lane, Princeton, NJ 08544, USA*
[7]*Steward Observatory, University of Arizona, 933 North Cherry Avenue, Tucson, AZ 85721, USA*
[8]*Dipartimento di Fisica, Università di Roma Tor Vergata, via Della Ricerca Scientifica 1, I-00133, Roma, Italy*
[9]*INAF, Rome Astronomical Observatory, via Frascati 33, I-00040, Monte Porzio Catone, Italy*
[10]*Leibniz-Institüt für Astrophysik Potsdam, An der Sternwarte 16, D-14482, Potsdam, Germany*
[11]*INAF-Osservatorio di Astrofisica e Scienza dello Spazio di Bologna, Via Gobetti 93/3, I - 40129, Bologna, Italy*
[12]*Division of Physics, Mathematics and Astronomy, California Institute of Technology, Pasadena, Ca., 91125*

[13]*Space Science Data Center - ASI, via del Politecnico, s.n.c., I-00133, Roma, Italy*
[14]*Department of Astronomy & Astrophysics, University of Chicago, 5640 South Ellis Avenue, Chicago, IL 60637, USA*
[15]*Dipartimento di Fisica e Astronomia, Università di Bologna, Via Gobetti 93/2, I - 40129, Bologna, Italy*
[16]*IPAC, Mail Code 314-6, Caltech, 1200 E. California Blvd., Pasadena, CA 91125, USA*
[17]*Department of Astronomy, University of Virginia, 530 McCormick Road, Charlottesville, VA 22904, USA*
[18]*Department of Physics and Astronomy, Iowa State University, A313E Zaffarano, Ames, IA 50010, USA*
[19]*National Optical Astronomy Observatory, 950 North Cherry Avenue, Tucson, AZ 85719, USA*
[20]*Nicolaus Copernicus Astronomical Center, Polish Academy of Sciences, Bartycka 18, 00-716 Warsaw, Poland*
[21]*Max Planck Institute for Astronomy, Konigstuhl 17, D-69117, Heidelberg, Germany*
[22]*Department of Physics and Astronomy, Michigan State University, East Lansing, MI 48824-2320, USA*
[23]*Warsaw University Observatory, Al. Ujazdowskie 4, 00-478 Warszawa, Poland*

This paper has been typeset from a TEX/LATEX file prepared by the author.